



Fine-tuning channel structure and surface chemistry of stable bismuth-organic frameworks for efficient C₂H₄ purification through reversely trapping CO₂ and C₂H₂

Chunlian Hao^a, Zhencui Ge^b, Rajamani Krishna^c, Hao Ren^a, Houyu Zhu^a, Yuhua Chi^a, Wen Zhao^a, Xiuping Liu^d, Wenye Guo^{a,*}

^a School of Materials Science and Engineering, China University of Petroleum, Qingdao, Shandong 266580, People's Republic of China

^b College of Science, China University of Petroleum, Qingdao, Shandong 266580, People's Republic of China

^c Van 't Hoff Institute for Molecular Sciences, University of Amsterdam, Science Park 904, 1098 XH Amsterdam, the Netherlands

^d School of Materials Science and Engineering, Linyi University, Linyi, Shandong 276000, People's Republic of China

ARTICLE INFO

Keywords:

Bismuth-organic frameworks
Surface structure/chemistry regulation
CO₂ recognition
C₂H₄ purification
Molecular simulations

ABSTRACT

One-step C₂H₄ purification from ternary C₂H₄/C₂H₂/CO₂ mixtures is of prime importance but challenging in chemical industries, owing to similar physicochemical properties of the three gases. Herein, we investigated the potential of ultramicroporous Bi-MOFs modified with -CHO, -COOH, -NO₂, -F, -Cl, -Br, and -I for C₂H₄ purification. These MOFs featured good thermodynamic and thermal stability and exhibited precise regulation of channel sizes and surface structures/electronegativity. Their separation performances for CO₂/C₂H₄, C₂H₂/C₂H₄, and CO₂/C₂H₂ were theoretically investigated by grand canonical Monte Carlo, density functional theory, and transient breakthrough simulations. Results showed that introducing -CHO/-COOH/-NO₂ enlarged the difference of adsorption uptakes between CO₂, C₂H₂, and C₂H₄ favoring efficient separation of corresponding mixtures, in which Bi-MOF-CHO showed the highest selectivity for CO₂/C₂H₄, C₂H₂/C₂H₄, and CO₂/C₂H₂, with values of 58.6 (64.5), 11.8 (11.5), and 7.7 (21.5) under 50/50 (1/99) at ambient conditions. The enhanced separation performance is attributed to the synergism of pore size limitation, fine-tuned surface structure, and high surface electronegativity, resulting in special CO₂ recognition, moderate enhancement for C₂H₂, but negligible influence on C₂H₄ adsorption. This work provides an effective strategy to design high-performance adsorbents for one-step C₂H₄ purification from ternary C₂H₄/C₂H₂/CO₂ mixtures.

1. Introduction

Ethylene (C₂H₄) is the most widely produced chemical, with an estimated global production of 158 million tons in 2020 and an expected annual growth rate of ~ 4.5% until 2027 [1,2]. It is mainly produced by steam cracking of petrochemicals, which is facing petroleum reserves shortage and high energy consumption [3]. Oxidative coupling of methane (OCM) has been proposed as an alternative by virtue of energy saving, low cost, and abundant availability of methane (CH₄). Apart from C₂H₄, OCM processes also produce byproducts acetylene (C₂H₂) and carbon dioxide (CO₂) [4,5], which need to be removed to obtain high-purity C₂H₄ for industrial applications [6]. Besides, C₂H₂ is also an important chemical/raw feedstock, emphasizing the need for its extraction from mixtures [7–10]. However, separating ternary C₂H₄/

C₂H₂/CO₂ mixtures is challenging due to their identical molecular dimensions and physical properties (Table S1) [11–13]. Current separation technologies, including solvent extraction and cryogenic distillations, are cost/energy intensive and environmentally unfriendly [14]. To mitigate the deficiencies, researchers are focusing on developing novel adsorbents with facile regeneration/recycling capability and significant affinity differences towards various components from gas mixtures [15,16].

Great advances have been made in light hydrocarbon separations by using metal-organic frameworks (MOFs) as adsorbents [17–20]. For C₂H₄ purification from ternary mixtures, one viable strategy is using synergistic sorbent separation technology under the synergism of multiple MOFs, each of which is selective for one component from mixtures, however, the interplay of packing sequence and gas mass transfer limits

* Corresponding author.

E-mail address: wgyuo@upc.edu.cn (W. Guo).

<https://doi.org/10.1016/j.cej.2023.144533>

Received 17 April 2023; Received in revised form 27 June 2023; Accepted 29 June 2023

Available online 30 June 2023

1385-8947/© 2023 Elsevier B.V. All rights reserved.

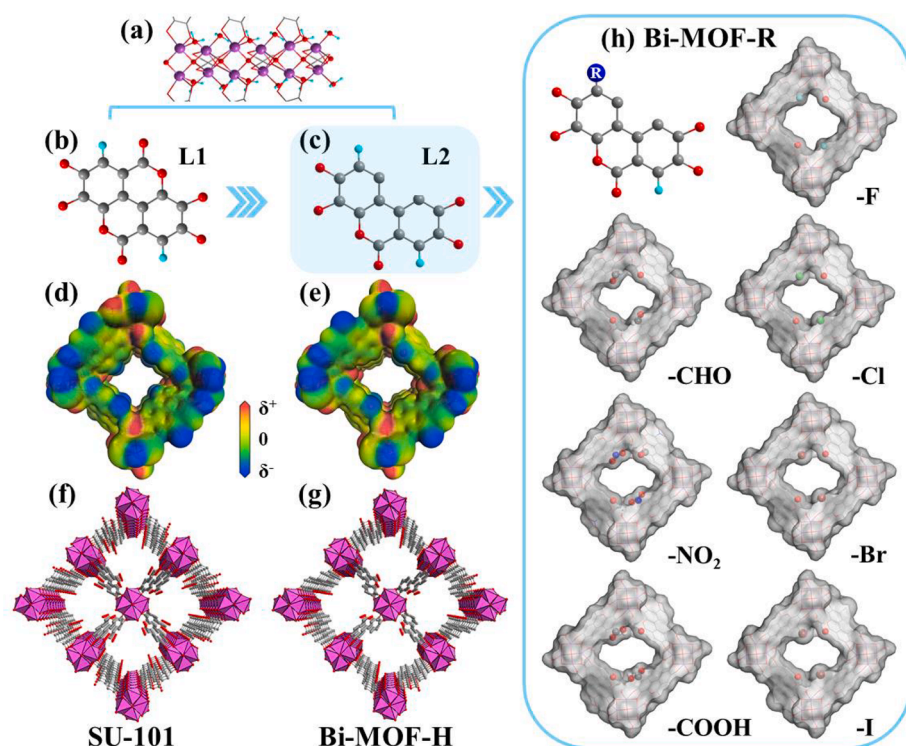


Fig. 1. Design of the modification method and illustration of crystal structures of Bi-MOFs. (a) Infinite secondary building units (iSBUs) in Bi-MOFs comprise one-dimensional Bi chains. C, H, O, and Bi atoms are represented by gray, light blue, red, and purple, respectively. (b,c) Structures of ellagic acid (L1) and urolithin D (L2). (d,e) Electrostatic potential maps of channel surfaces in SU-101 and Bi-MOF-H. The isovalue of electron density distribution is $0.017 \text{ e}/\text{\AA}^3$. (f,g) Structures of SU-101 and Bi-MOF-H with 1D channels. (h) Structure of functionalized linker L2 and Connolly surfaces of functionalized Bi-MOF frameworks with the Connolly radii of 1.0 \AA ($R = -F, -Cl, -Br, -I, -CHO, -NO_2, \text{ and } -COOH$).

its practical application [11,21]. Therefore, it is more efficient and maneuverable to develop a novel adsorbent realizing one-step C_2H_4 purification via simultaneously extracting impurities CO_2 and C_2H_2 from $C_2H_4/C_2H_2/CO_2$ mixtures [21,22]. To fulfill the task, the required adsorbent should simultaneously have strong affinity toward C_2H_2 and CO_2 but weak C_2H_4 affinity. Based on a survey of reported MOFs with C_2H_4 purification performance, we find that a certain number of MOFs can separate C_2H_2/C_2H_4 efficiently [24–26], yet relevant research is still in the ascendant; on the other hand, the MOFs that can selectively adsorb CO_2 from C_2H_4 have been rarely reported, due to the lower CO_2 polarizability than that of C_2H_4 and lack of a clear separation mechanism [23]. Based on the analysis above, it will be more complex and challenging to develop a MOF adsorbent, that can trap CO_2 and C_2H_2 simultaneously from ternary mixtures for one-step C_2H_4 purification; and to date, only a few successful examples include SIFSIX-17-Ni [24], TiFSIX-17-Ni [24], Zn-atz-oba [25], and ZNU-6 [26].

Recently, we chose Bi-based SU-101 as the CO_2 -selective adsorbent platform [27], because of the excellent stability, ultramicropores, and rich carbonyl O sites, as well as the non-toxicity, low cost, and environment friendliness of bismuth [28–30]. Then the isostructural SU-101 (M) (M = Bi, In, Ga, and Al) materials with square channels were obtained [27], in which pore size confinement and surface O_{Carbonyl} atoms

synergistically facilitated the surface electrostatic potential complementary to CO_2 molecule but incompatible with C_2H_2 and C_2H_4 , realizing the selective adsorption of CO_2 over C_2H_2 and C_2H_4 , but unable to distinguish the latter two. Therefore, although SU-101(M) materials are CO_2 favored, they are not suitable for one-step C_2H_4 purification from $C_2H_4/C_2H_2/CO_2$ mixtures. This might be improved by regulating the ligand structure and functionalization of SU-101, so that the channel shape/size and surface chemistry of the new materials facilitate an enhanced uptake of C_2H_2 and meanwhile maintain the adsorption character of both C_2H_4 and CO_2 .

Based on the above consideration, in this work, we built a series of novel isostructural Bi-MOFs, featuring lower-symmetry and non-square (plump-shaped) channels, by replacing the ellagic acid ligand (L1) in SU-101(Bi) with low-symmetry urolithin D (L2) and its functionalized derivatives (containing $-CHO, -COOH, -NO_2, -F, -Cl, -Br,$ and $-I$), for precise control of channel sizes/structures and surface electrical properties (Fig. 1). We investigated the C_2H_4 purification performance from CO_2/C_2H_4 and C_2H_2/C_2H_4 together with corresponding intrinsic mechanisms in functionalized Bi-MOFs by grand canonical Monte Carlo (GCMC) and density functional theory (DFT). Thereinto, Bi-MOF-CHO/ $-COOH/-NO_2$ not only exhibited high CO_2/C_2H_4 and C_2H_2/C_2H_4 selectivities but also showed efficient CO_2/C_2H_2 separation, thanks to the

Table 1

Summary of physical characteristics, charge (q) of exposed functional-group electronegative atoms, cohesive energy (E_{coh}), and formation energy (E_{form}) of Bi-MOFs.

	-H	-CHO	-NO ₂	-COOH	-F	-Cl	-Br	-I
ρ^a	2.6	2.7	2.7	2.7	2.6	2.7	2.8	3.0
D_{PL}^b	6.41	4.80	4.88	4.72	6.25	5.25	4.87	4.42
D_{LC}^c	7.51	5.80	6.24	5.99	6.86	6.39	6.00	5.46
V_p^d	0.12	0.08	0.08	0.09	0.12	0.10	0.09	0.08
q_{O}^e	-0.52	-0.55	-0.55	-0.53	-0.53	-0.51	-0.50	-0.50
q_X^f		-0.44	-0.46	-0.52	-0.17	-0.10	-0.03	-0.04
			-0.58					
E_{coh}^g	6.8	6.9	6.9	6.9	6.8	6.8	6.8	6.8
E_{form}^h	-2.66	-2.63	-2.50	-2.62	-2.64	-2.58	-2.58	-2.59

^a Crystal density (g/cm^3). ^b Pore limiting diameter (PLD, \AA). ^c Largest cavity diameter (LCD, \AA). ^d Available pore volume (cm^3/g). ^e Charge of carbonyl O atom. ^f Charge of X (electronegative atom: O, F, Cl, Br, and I) from functional groups exposed to channel surfaces. ^g Cohesive energy (eV/atom). ^h Formation energy (eV/atom).

fine-tuned MOF structures, ultramicroporous channels, and surface electronegativity exerted by functional groups. Further, we also evaluated the productivities of polymer grade C₂H₄ (purity > 99.996%) from the 1/1/98 and 1/9/90 C₂H₂/CO₂/C₂H₄ ternary mixtures purified with Bi-MOF-CHO/-COOH/-NO₂ by transient breakthrough simulations. This work provides general guidance for designing stable adsorbents for one-step C₂H₄ purification from ternary C₂H₄/C₂H₂/CO₂ mixtures.

2. Simulation details

2.1. Structure design

Based on SU-101(Bi) [27], we first constructed the isostructural Bi-MOF-H by replacing ligand L1 with L2 (Fig. 1a–g). This led to missing of half of the carbonyl groups on channel surface, which is featured by a lower-symmetrical non-square shape with enlarged pore size of 7.52 Å (vs. 6.8 Å in SU-101(Bi)) [30]; then, various functional groups (R = -F, -Cl, -Br, -I, -CHO, -COOH, and -NO₂) containing exposed electronegative atom(s) were introduced in L2 to make up the missing carbonyl groups. The obtained functionalized Bi-MOFs (named Bi-MOF-R) featured decreased pore sizes (5.46 ~ 6.86 Å, Table 1) and different non-square shapes of 1D functionalized channels, exhibiting fine-tuned channel structures and surface electronegativity driven by functional groups (Figs. 1h and S1). The structural parameters of Bi-MOFs are presented in Table 1, which are calculated by zeo++ software [31,32] using N₂ probe.

2.2. Density functional theory (DFT) calculations

DFT calculations were performed to obtain the atomic partial charges, electrostatic potentials, and stable adsorption configurations and energies by using the Dmol³ module [33]. Generalized gradient approximation (GGA) with the Perdew-Burke-Ernzerhof (PBE) functional was used to do all-electron spin-unrestricted DFT calculations. Tkatchenko-Scheffler (TS) correction method was employed to account for the vdW interactions [34]. The double numerical including polarization (DNP) basis set was chosen for all atoms. The adsorption energy (ΔE_{ads}) was calculated based on the following equation:

$$\Delta E_{ads} = E_{sorbent} + E_{gas} - E_{total} \quad (1)$$

where $E_{sorbent}$, E_{gas} , and E_{total} are the total energies of the sorbent framework, gas molecule, and gas-sorbent adsorption system, respectively.

Cohesive energy and formation energy were calculated using Vienna Ab initio Simulation Package [35–37]. A plane-wave cutoff energy of 500 eV and $1 \times 1 \times 1$ Gamma-center k -point were adopted for all calculations. The electronic energy was converged to within 10^{-6} eV and the force on each atom was less than 0.02 eV/Å. The cohesive energy (E_{coh}) represented the required energy to decompose a MOF framework into isolated atoms, calculated by the formula [38,39]:

$$E_{coh} = \left(\sum n_i E_i - E_{fram} \right) / \sum n_i \quad (2)$$

where E_i and E_{fram} represent the total energies of isolated atom i and MOF framework, and n_i is the number of atom i in the MOF framework. The formation energy (E_{form} , eV/atom) of Bi-MOFs was expressed as [40,41]:

$$E_{form} = (E_{fram} - \sum n_i \mu_i) / \sum n_i \quad (3)$$

where μ_i is the chemical potential of atom i in Bi-MOF frameworks. The thermal stability of Bi-MOFs was examined with the simulation time of 5000 fs based on the Nosé-Hoover method using Ab-initio molecular dynamics (AIMD) simulations [42].

2.3. Grand canonical Monte Carlo (GCMC) simulations

GCMC simulations were carried out to evaluate the adsorption and separation performance of Bi-MOFs by using the multipurpose simulation code [43]. The simulation box (containing $2 \times 2 \times 5$ unit cells) of Bi-MOFs was kept rigid and periodic boundary conditions were applied in all three dimensions. The Lennard-Jones (L-J) and electrostatic interactions were combined to describe gas-gas and gas-framework interactions. The cutoff of 12 Å was employed for L-J interaction and electrostatic interaction was described by Ewald summation. For each pressure point, the first 40% of 8×10^7 steps were used to guarantee the system equilibration, and the remaining steps were implemented to obtain the desired thermodynamic properties.

CO₂ and C₂H₂ were modeled as rigid linear molecules, and C₂H₄ was modeled as a rigid three-site model, including two CH₂ groups and one pseudoatom at the center of mass (COM) [44–46]. For Bi-MOFs, the universal force field (UFF) [47] and Dreiding force field [48] are used for metal and non-metal atoms, respectively. Details of force field parameters and atomic partial charges for adsorbates and MOFs are provided in Table S3 and Fig. S2. In addition to the force field validation demonstrated in our previous work [27,49,50], the force field parameters have also been extensively employed in reproducing experimental adsorption isotherms and conducting mechanism analysis for synthesized MOFs [51–54], making performance prediction [55–59], and providing theoretical guidance for the rational design and synthesis of MOFs [60–63]. The cross-interaction parameters between different atoms were calculated by Lorentz-Berthelot mixing rules:

$$\varepsilon_{ij} = \sqrt{\varepsilon_i \varepsilon_j}, \sigma_{ij} = (\sigma_i + \sigma_j) / 2 \quad (4)$$

For binary mixtures, the adsorption selectivity ($S_{i/j}$) of component i over component j was derived from:

$$S_{i/j} = \frac{x_i/x_j}{y_i/y_j} \quad (5)$$

where x_i (x_j) and y_i (y_j) are the molar fractions of component i (j) in adsorbed phase and bulk gas phase, respectively.

3. Results and discussion

3.1. Structural analysis and performance prediction

Fig. 1h shows that carbonyl and functional groups are distributed diagonally in channels, making the surface structure and chemistry differ significantly across various Bi-MOFs. In Bi-MOF-CHO/-COOH/-NO₂ shown in Fig. S3b–d, the distances between O_{CHO/-NO₂/-COOH} (i.e., atom X) and O1/O2 from carbonyl groups are 6.10 ~ 6.29/5.14 ~ 5.30 Å, larger than those in Bi-MOF-F/-Cl/-Br/-I (5.33 ~ 5.57/4.27 ~ 4.90 Å for X-O1/O2; see Fig. S3e–h). Oppositely, the X-O3 and X-O4 distances in Bi-MOF-CHO/-COOH/-NO₂ are 7.00 ~ 7.03 and 7.75 ~ 7.78 Å, respectively, smaller than those in Bi-MOF-F/-Cl/-Br/-I (7.69 ~ 8.29 and 8.23 ~ 8.71 Å). Therefore, a plumper region by carbonyl and functional groups can be formed in Bi-MOF channels modifying with -CHO, -NO₂, and -COOH, as compared to the situation of the halogen substitution (Fig. 1h). In addition to facilitating interaction with CO₂, these plump spaces in Bi-MOF-CHO/-COOH/-NO₂ are expected to favor multiple-site recognition of linear C₂H₂ but not for plane C₂H₄, as comparing the X-O3/O4 distances (7.00 ~ 7.78 Å) with the dimensions of the molecules (Table S1).

Owing to the crucial importance of structural stability in practical applications, we explored the stability of Bi-MOFs from the following aspects. First, the Bi-O bond lengths of Bi-MOFs (2.13 ~ 2.22 Å) are similar with those in synthesized SU-101(Bi) (2.1 ~ 2.3 Å) and shorter than those in reported carboxyl-based Bi-MOFs (2.4 ~ 2.8 Å) [30]. This indicates the strong metal-ligand bond strengths resulting in good thermodynamic stability of Bi-MOFs. Second, the cohesive energy (E_{coh})

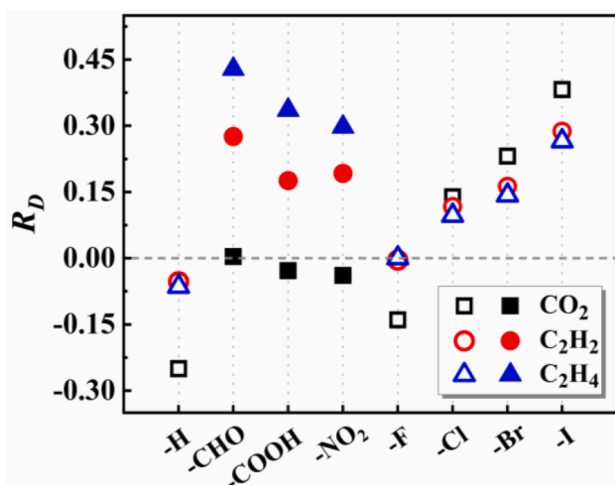


Fig. 2. The comparison of R_D values for CO_2 , C_2H_2 , and C_2H_4 adsorption in Bi-MOFs. $R_D = \ln(2D/D_{LC})$, where D represents the DFT-calculated equilibrium distance between gas and framework (see Fig. S5 for details) and D_{LC} is the largest cavity diameter of corresponding Bi-MOF (Table 1) ($R_D > 0$: repulsive adsorption; $R_D \leq 0$: attractive adsorption).

values of Bi-MOFs are calculated to be 6.8–6.9 eV/atom (Table 1), which are comparable to or even larger than that of many stable MOFs, such as Zn-BTC (6.93 eV/atom) [64], Zr-MOF-525 (5.36 eV/atom) [65], and Hf-MOF-525 (5.47 eV/atom) [65], revealing the good stability of these Bi-MOFs. Next, the negative formation energy (E_{form}) ($-2.50 \sim -2.66$ eV/atom) of Bi-MOFs is comparable to that of synthesized SU-101(Bi) (-2.64 eV/atom), suggesting their formation is thermodynamically favorable (Table 1). Finally, AIMD simulations were performed to prove the good thermal stability of Bi-MOFs, showing the structural integrity of Bi-MOFs could well maintain at 300 K, and meanwhile, the energy only fluctuated over time in a narrow range (Fig. S4).

We have previously explained the opposite adsorption properties for CO_2 (attractive) and $\text{C}_2\text{H}_2/\text{C}_2\text{H}_4$ (repulsive) in SU-101 materials by comparing adsorbate- $\text{O}_{\text{Carbonyl}}$ distances with channel radius [27]. To roughly estimate the adsorption property for gas separation, we define $R_D = \ln[D/(D_{LC}/2)] = \ln(2D/D_{LC})$, where D represents the minimum equilibrium distance of the gas molecule at surface adsorption sites and D_{LC} is the largest cavity diameter of corresponding adsorbent. If $R_D > 0$,

the gas tends to be adsorbed repulsively, otherwise it will be attractively. As shown in Fig. 2, the R_D values in Bi-MOF-H and Bi-MOF-F follow the order of $R_D(\text{CO}_2) < R_D(\text{C}_2\text{H}_2) \approx R_D(\text{C}_2\text{H}_4) \leq 0$, showing the attractive adsorption for the three gases; while in Bi-MOF-Cl/-Br/-I, the opposite order of $R_D(\text{CO}_2) > R_D(\text{C}_2\text{H}_2) \approx R_D(\text{C}_2\text{H}_4) > 0$ shows the repulsive adsorption for the three gases; and the close R_D values together with no strong attractive adsorption of specific gases indicate that it is hard to distinguish the three gases with above Bi-MOFs. For Bi-MOF-CHO/-COOH/- NO_2 , however, the larger divergence of R_D values for CO_2 ($-0.04 \sim 0.00$), C_2H_2 ($0.18 \sim 0.28$), and C_2H_4 ($0.30 \sim 0.43$) not only demonstrates the attractive adsorption for CO_2 and repulsive ones for $\text{C}_2\text{H}_2/\text{C}_2\text{H}_4$, but also predicts the different affinities toward the three gases as well as the potential for $\text{CO}_2/\text{C}_2\text{H}_2/\text{C}_2\text{H}_4$ separation.

3.2. Single-component gas adsorption

Fig. 3a–c presents the absolute adsorption isotherms of C_2H_4 , C_2H_2 , and CO_2 in Bi-MOF materials at 298 K, together with those of Bi-based SU-101 for comparison. We can find that all the adsorption isotherms exhibit the Type-I adsorption character. The substitution of ligand L2 (Bi-MOF-H) for L1 (SU-101) could significantly and slightly enhance C_2H_4 and C_2H_2 adsorption, respectively, but negligibly affects CO_2 adsorption. The $\text{C}_2\text{H}_4/\text{C}_2\text{H}_2/\text{CO}_2$ uptakes at 100 kPa are changed from 58.5/138.4/145.0 cm^3/cm^3 (SU-101) to 91.2/131.5/147.2 cm^3/cm^3 (Bi-MOF-H), exhibiting a similar increase trend of the adsorption isotherms in the two materials. Except CO_2 adsorption in Bi-MOF-F, the functionalization of ligand L2 can greatly impact the adsorption of CO_2 , C_2H_2 , and C_2H_4 in Bi-MOFs, giving a gentler increase trend in the adsorption isotherms, through enhancing and suppressing the adsorption uptakes at the low and high pressures, respectively.

Fig. 3a shows that functionalization in Bi-MOFs slightly enhances C_2H_4 adsorption at low pressures, but decreases it mildly at high pressures, with the uptakes of 4.7 ~ 10.7 cm^3/cm^3 at 1 kPa and 71.2 ~ 82.0 cm^3/cm^3 at 100 kPa. For C_2H_2 adsorption (Fig. 3b), Bi-MOF-CHO shows the largest uptake of 56.6 ~ 81.8 cm^3/cm^3 between 1 ~ 100 kPa, while other functionalized Bi-MOFs exhibit lower uptakes (9.6 ~ 18.8 cm^3/cm^3) at low pressures and comparable uptakes (72.1 ~ 92.1 cm^3/cm^3) at high pressures. For CO_2 adsorption (Fig. 3c), Bi-MOF-CHO exhibits the largest uptakes (77.1 ~ 147.7 cm^3/cm^3 , 1 ~ 100 kPa), followed by Bi-MOF- NO_2 (16.1 ~ 129.1 cm^3/cm^3) and Bi-MOF-COOH (33.7 ~ 114.7 cm^3/cm^3). Bi-MOF-F exhibits similar uptake-pressure relation as Bi-MOF-H for CO_2 adsorption (5.9 ~ 147.0 cm^3/cm^3), while introducing

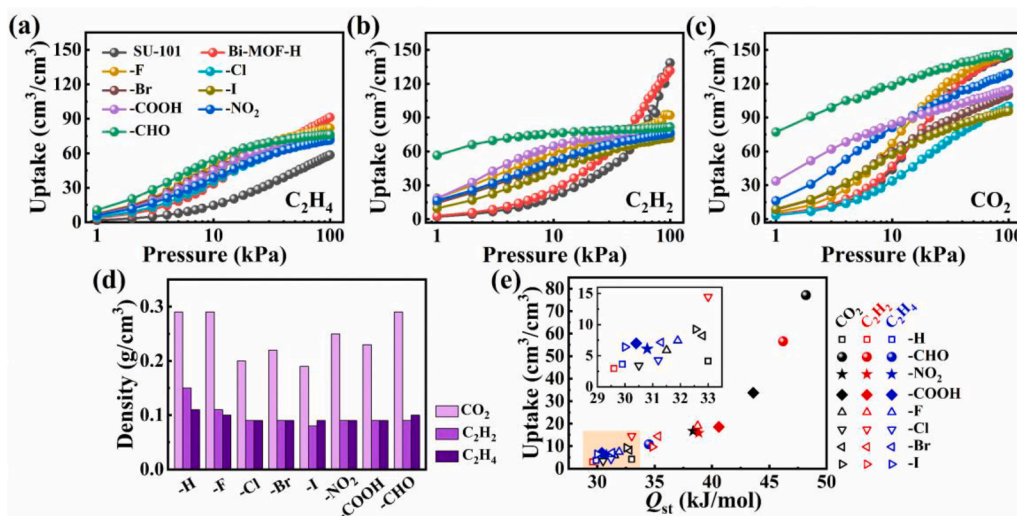


Fig. 3. (a–c) Adsorption isotherms of C_2H_4 , C_2H_2 , and CO_2 in SU-101 and Bi-MOF materials at 298 K and up to 100 kPa. (d) The mass densities of adsorbed CO_2 , C_2H_2 , and C_2H_4 at 298 K and 100 kPa in Bi-MOF materials obtained based on framework volumes. (e) The uptakes of CO_2 , C_2H_2 , and C_2H_4 at 298 K and 1 kPa as a function of initial affinity (Q_{st}) for Bi-MOF materials. Note that 1 cm^3/cm^3 is equal to 1 cc/cc.

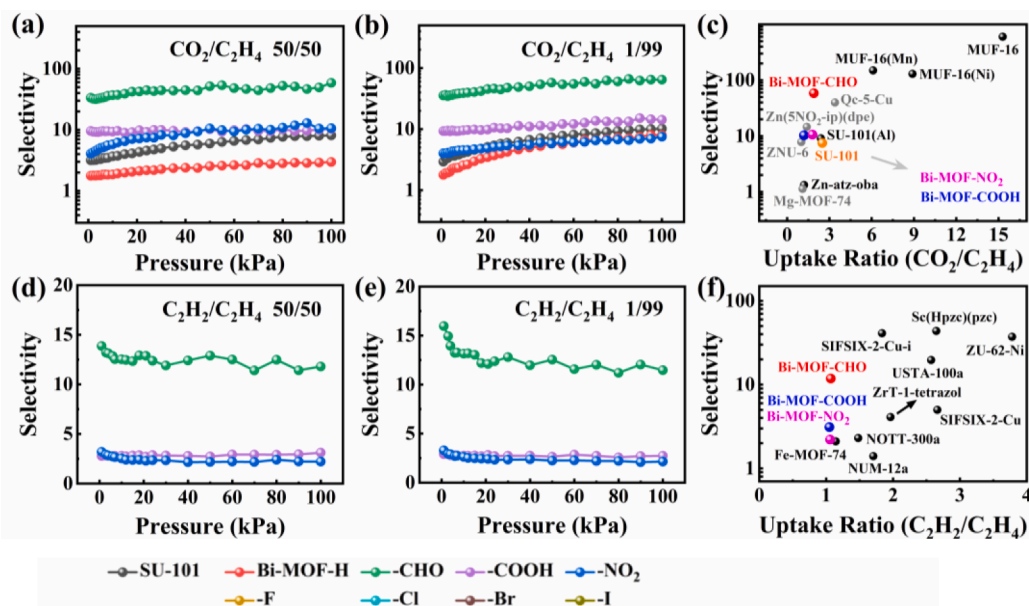


Fig. 4. Selectivities of (a,b) $\text{CO}_2/\text{C}_2\text{H}_4$ and (d,e) $\text{C}_2\text{H}_2/\text{C}_2\text{H}_4$ in Bi-MOFs at 298 K under 50/50 and 1/99. (c,f) Comparison of the selectivity and corresponding uptake ratio for equimolar $\text{CO}_2/\text{C}_2\text{H}_4$ and $\text{C}_2\text{H}_2/\text{C}_2\text{H}_4$ between functionalized Bi-MOFs and other top-performance MOFs at atmospheric temperatures [11,25–27,69–78].

-Cl, -Br, and -I decreases the CO_2 uptakes with values between $3.4 \sim 8.9 \text{ cm}^3/\text{cm}^3$ (1 kPa) and $95.7 \sim 110.3 \text{ cm}^3/\text{cm}^3$ (100 kPa). The mass densities of adsorbed gases based on framework volumes in the Bi-MOF frameworks are calculated to intuitively display the adsorption ability of Bi-MOFs (Fig. 3d), with the values of $0.20 \sim 0.29 \text{ g}/\text{cm}^3$ for CO_2 and $0.09 \sim 0.15 \text{ g}/\text{cm}^3$ for C_2H_2 and C_2H_4 at 100 kPa. The ultrahigh CO_2 adsorption densities in Bi-MOFs are comparable to those of the compressed CO_2 at 6000 \sim 8000 kPa and room temperature [66]; the adsorption densities of all three gases are two orders of magnitude higher than those at standard temperature and pressure (1.98×10^{-3} , 1.16×10^{-3} , and $1.25 \times 10^{-3} \text{ g}/\text{cm}^3$ for CO_2 , C_2H_2 , and C_2H_4) [67], revealing the efficient dense packing of gases in Bi-MOFs. During the C_2H_4 production process, traces of impurity C_2H_2 are always produced inevitably, which can poison Ziegler-Natta catalysts and lower the quality of downstream products obtained from C_2H_4 polymerization [68,69]. To meet the requirement, C_2H_4 as the feedstock should be subjected to pre-purification so that the content of C_2H_2 becomes less than 40 ppm [68,69], which drives us to perform GCMC simulations below 1 kPa. Fig. S6a–c shows the CO_2 and C_2H_2 uptakes are larger than that of C_2H_4 in Bi-MOF-CHO/–COOH/– NO_2 in 2 \sim 1000 Pa. In particular below 4 Pa (Fig. S6d–f), compared with almost zero C_2H_4 adsorption, only Bi-MOF-CHO exhibits significant adsorption for CO_2 and C_2H_2 , showing the potential for $\text{CO}_2/\text{C}_2\text{H}_4$ and $\text{C}_2\text{H}_2/\text{C}_2\text{H}_4$ separation.

Fig. 3e shows that the adsorption heats (Q_{st}) of gases in Bi-MOFs are positively correlated with their low-pressure uptakes. Among all Bi-MOFs, Bi-MOF-CHO exhibits the largest low-pressure uptakes and Q_{st} (in cm^3/cm^3 and kJ/mol) in sequence of CO_2 (77.1/48.2) > C_2H_2 (56.6/46.2) > C_2H_4 (10.7/34.6); Bi-MOF-COOH shows the similar sequence CO_2 (33.7/43.6) > C_2H_2 (18.5/40.6) > C_2H_4 (6.4/30.6), and the order in Bi-MOF- NO_2 is CO_2 (16.1/38.8) \approx C_2H_2 (16.6/38.5) > C_2H_4 (6.2/30.7). Halogen-modified Bi-MOFs show better adsorption performance for C_2H_2 than CO_2 and C_2H_4 (see details in Fig. S7), but in general, the difference between the three gases is very small for both the uptakes and Q_{st} values, consistent with the prediction shown in Fig. 2. To sum up, Bi-MOFs-CHO/–COOH/– NO_2 differs greatly in adsorption abilities for C_2H_4 , C_2H_2 , and CO_2 and shows potential separation performance for $\text{CO}_2/\text{C}_2\text{H}_4$, $\text{C}_2\text{H}_2/\text{C}_2\text{H}_4$, and $\text{CO}_2/\text{C}_2\text{H}_2$.

3.3. Separation of gas mixtures

To evaluate the separation performance of Bi-MOFs, GCMC simulations were performed for $\text{CO}_2/\text{C}_2\text{H}_4$, $\text{C}_2\text{H}_2/\text{C}_2\text{H}_4$, and $\text{CO}_2/\text{C}_2\text{H}_2$ mixtures at 298 K (Figs. 4 and S8). Compared to SU-101, Bi-MOF-H exhibits significantly decreased selectivities of $\text{CO}_2/\text{C}_2\text{H}_2$ and $\text{CO}_2/\text{C}_2\text{H}_4$, with values of 3.7 (3.4) and 3.0 (7.9) under 50/50 (1/99) and 100 kPa. However, this disadvantage can be modified by ligand functionalization. Introducing –CHO/–COOH/– NO_2 efficiently improves the separation of CO_2 from C_2H_4 and C_2H_2 , well consistent with the fact that –CHO/–COOH/– NO_2 can enlarge the difference in adsorption amounts between different components from equimolar $\text{CO}_2/\text{C}_2\text{H}_4$ and $\text{CO}_2/\text{C}_2\text{H}_2$ mixtures (Fig. S9b–d). Unlike SU-101 beneficial for $\text{CO}_2/\text{C}_2\text{H}_2$ separation [27], Bi-MOF-CHO/–COOH/– NO_2 is more conducive to separate $\text{CO}_2/\text{C}_2\text{H}_4$ and also shows additional $\text{C}_2\text{H}_2/\text{C}_2\text{H}_4$ separation performance, which is the key improvement of our new materials for one-step C_2H_4 purification. However, introducing halogen groups leads to only a negligible or even negative effect on $\text{CO}_2/\text{C}_2\text{H}_4$ and $\text{CO}_2/\text{C}_2\text{H}_2$ separation, and completely fails to separate $\text{C}_2\text{H}_2/\text{C}_2\text{H}_4$. Besides, the selectivity of binary mixtures is not substantially dependent on the component ratios, but varies differently for different mixtures, especially under 1/99, showing a nearly linear increase relation with pressure for $\text{CO}_2/\text{C}_2\text{H}_4$, ramp-up tendency for $\text{CO}_2/\text{C}_2\text{H}_2$, and ramp-down for $\text{C}_2\text{H}_2/\text{C}_2\text{H}_4$.

At 100 kPa, Bi-MOFs modified with –CHO, –COOH, – NO_2 , and halogen exhibit equimolar $\text{CO}_2/\text{C}_2\text{H}_4$ selectivity of 58.6, 10.6, 10.3, and 2.1 \sim 4.3, respectively, and slightly increase to 64.5, 14.2, 7.5, and 1.7 \sim 3.9 under 1/99. In Bi-MOF-CHO/–COOH/– NO_2 , the $\text{C}_2\text{H}_2/\text{C}_2\text{H}_4$ selectivities are 11.8/3.1/2.2 (50/50) and 11.5/2.7/2.1 (1/99) at 100 kPa. Besides, the functionalized Bi-MOFs only show moderate $\text{CO}_2/\text{C}_2\text{H}_2$ separation performance, with the selectivity no more than 7.7 at 100 kPa, except for Bi-MOF-CHO (21.5) under 1/99 (Fig. S8). We also calculated the IAST selectivity of Bi-MOF-CHO/–COOH/– NO_2 based on single gas adsorption isotherms in Fig. 3a–c, and found that the IAST selectivity of equimolar $\text{CO}_2/\text{C}_2\text{H}_4$ and $\text{C}_2\text{H}_2/\text{C}_2\text{H}_4$ (Fig. S10) is highly consistent with the GCMC calculated results (Fig. 4a,d), whether in the growth trend or in the range of values. As is well-known, light hydrocarbon mixtures always contain contaminants, such as hydrogen sulfide (H_2S) [59], which not only has a great harm to the human health even in very low concentrations (300 ppm), but also deactivates the catalysts and corrodes the equipment [79]. The calculated adsorption uptakes of

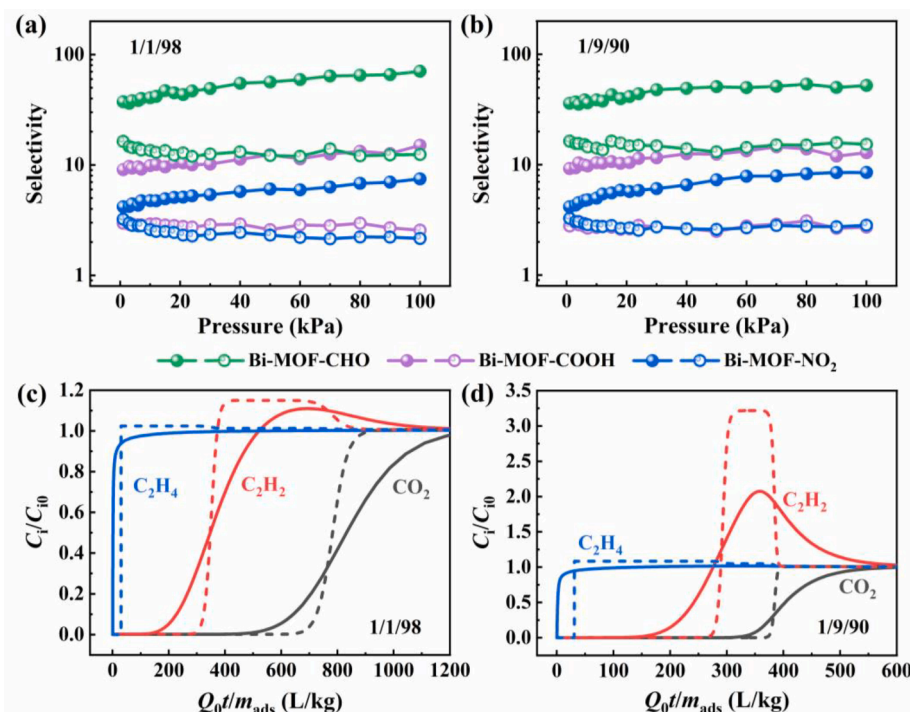


Fig. 5. (a, b) The selectivity of $\text{CO}_2/\text{C}_2\text{H}_4$ (Solid ball) and $\text{C}_2\text{H}_2/\text{C}_2\text{H}_4$ (Open ball) from ternary 1/1/98 and 1/9/90 $\text{C}_2\text{H}_2/\text{CO}_2/\text{C}_2\text{H}_4$ mixtures in Bi-MOF-CHO/-COOH/- NO_2 at 298 K. (c, d) Transient breakthrough simulations for 1/1/98 and 1/9/90 $\text{C}_2\text{H}_2/\text{CO}_2/\text{C}_2\text{H}_4$ mixtures in the fixed bed packed with Bi-MOF-CHO at 298 K. The continuous solid lines represent simulations in which due account is taken of diffusional influences. The dashed lines are the simulations in which diffusional influences are considered to be negligible.

ternary $\text{H}_2\text{S}/\text{CO}_2/\text{C}_2\text{H}_4$ and $\text{H}_2\text{S}/\text{C}_2\text{H}_2/\text{C}_2\text{H}_4$ mixtures at 298 K (Fig. S11) show that H_2S has little influence on adsorbate uptakes in Bi-MOF-CHO/-COOH/- NO_2 during the separation processes of $\text{CO}_2/\text{C}_2\text{H}_4$ and $\text{C}_2\text{H}_2/\text{C}_2\text{H}_4$; and Bi-MOF-CHO/-COOH/- NO_2 only adsorb a small amount of H_2S during the separation processes.

Among all Bi-MOFs, Bi-MOF-CHO shows the largest equimolar $\text{CO}_2/\text{C}_2\text{H}_4$ selectivity (58.6, 100 kPa), which is only lower than benchmark MUF-16 materials (130 ~ 600) [70], but sits above most other $\text{CO}_2/\text{C}_2\text{H}_4$ -separation-used MOFs, such as Qc-5-Cu (39.95, 1/99) [11], Zn (5NO₂-ip)(dpe) (14.56, 1/99) [71], and SU-101(Al) (8.3) [27] (see Fig. 4c). As shown in Fig. 4f, Bi-MOF-CHO also shows a higher $\text{C}_2\text{H}_2/\text{C}_2\text{H}_4$ selectivity (11.8, 50/50) than many famous MOFs, such as NOTT-300 (2.3) [72], SIFSIX-2-Cu (5.0) [73], and Fe-MOF-74 (2.1) [74], but lower than the top-performance MOFs including [Sc(Hpzc)(pzc)] (43.6) [75], SIFSIX-2-Cu-i (41) [73], and ZU-62-Ni (37.2) [76]. Despite superior separation performance for binary mixtures, the reported adsorbents may be challenging to separate $\text{C}_2\text{H}_4/\text{C}_2\text{H}_2/\text{CO}_2$ mixtures through a single material [24]. For example, MUF-16 materials can separate $\text{CO}_2/\text{C}_2\text{H}_4$ efficiently but show comparable adsorption performances for C_2H_4 and C_2H_2 [70]. Unexpectedly, Bi-MOF-CHO/-COOH/- NO_2 , especially Bi-MOF-CHO, could simultaneously separate $\text{CO}_2/\text{C}_2\text{H}_4$, $\text{C}_2\text{H}_2/\text{C}_2\text{H}_4$, and $\text{CO}_2/\text{C}_2\text{H}_2$, showing the potential of one-step C_2H_4 purification from $\text{C}_2\text{H}_4/\text{C}_2\text{H}_2/\text{CO}_2$ mixtures.

In order to show directly the separation performance of Bi-MOF-CHO/-COOH/- NO_2 , we also performed GCMC simulations for two ternary $\text{C}_2\text{H}_2/\text{CO}_2/\text{C}_2\text{H}_4$ (1/1/98 and 1/9/90) mixtures, which are generally presented in oxidative coupling of methane [80,81]. Fig. 5a,b shows the selectivity of $\text{CO}_2/\text{C}_2\text{H}_4$ and $\text{C}_2\text{H}_2/\text{C}_2\text{H}_4$ calculated from the ternary mixtures is strictly analogous to that from the binary mixtures (Fig. 4), which predicts Bi-MOF-CHO the best-performance adsorbent, followed by Bi-MOF-COOH and Bi-MOF- NO_2 . For the 1/1/98 $\text{C}_2\text{H}_2/\text{CO}_2/\text{C}_2\text{H}_4$ mixture, the selectivities of $\text{CO}_2/\text{C}_2\text{H}_4$ (70.5/15.0/7.5, 100 kPa) and $\text{C}_2\text{H}_2/\text{C}_2\text{H}_4$ (12.5/2.6/2.2, 100 kPa) in Bi-MOF-CHO/-COOH/- NO_2 are comparable to those of 1/99 binary mixtures (Fig. 4b,e). Changing the ratio of gases to 1/9/90, the selectivity of Bi-MOF-CHO/-COOH/- NO_2 changes to a small extent, with the values of 52.1/12.8/8.5 ($\text{CO}_2/\text{C}_2\text{H}_4$) and 15.3/2.7/2.8 ($\text{C}_2\text{H}_2/\text{C}_2\text{H}_4$) at 100 kPa.

Transient breakthrough simulations for $\text{C}_2\text{H}_2/\text{CO}_2/\text{C}_2\text{H}_4$ (1/1/98

and 1/9/90) mixtures on Bi-MOF-CHO/-COOH/- NO_2 in a fixed bed were carried out at 298 K and $P_t = 10^5$ Pa total pressure, with the methodology described in earlier works of Krishna [82,83]. Only a brief description of the breakthrough simulations is given in Section S2. The simulations show that in all three Bi-MOFs, C_2H_4 is first detected at the outlet, followed by C_2H_2 , and CO_2 is retained in bed for the longest time (Figs. 5c,d, S14, and S15), in accordance with the sequence of the uptake abilities (Fig. 3a-c); also, intra-crystalline diffusion is expected to affect adversely the productivity of purified C_2H_4 , because it shortens the time intervals between the breakthrough points of C_2H_4 and C_2H_2 . Considering the intra-crystalline diffusion, the time interval in Bi-MOF-CHO is the maximum; and the productivities of polymer grade C_2H_4 (>99.996%) for 1/1/98 and 1/9/90 $\text{C}_2\text{H}_2/\text{CO}_2/\text{C}_2\text{H}_4$ mixtures are also the largest, with the values of 6.1 mol/kg (400.41 cm^3/cm^3) and 5.2 mol/kg (341.33 cm^3/cm^3), respectively, showing the best one-step C_2H_4 purification performance, among the three Bi-MOFs simulated (Tables S8 and S9). The C_2H_4 productivity of Bi-MOF-CHO under 1/9/90, the most reported ratio for $\text{C}_2\text{H}_2/\text{CO}_2/\text{C}_2\text{H}_4$ separations, is only lower than the top-performance MOFs, such as ZNU-6 (13.81 mol/kg or 367.39 cm^3/cm^3) [26], but is higher than most reported materials [24,26,80] (Table S10). Note that if volumetric productivities are considered (important for separator sizes), Bi-MOF-CHO shows a more obvious advantage (see Table S10), due to the higher density of Bi-containing MOFs with ultramicropores (Table 1).

3.4. Packing pattern for single-component gases and gas mixtures

From the snapshots in Fig. 6, CO_2 , C_2H_2 , and C_2H_4 all tended to adsorb on channel surfaces in Bi-MOF-H, verifying the attractive adsorption predicted in Fig. 2. Besides, the relative concentration of three gases showed only one broad peak in Bi-MOF-H channels along the a -axis (Fig. 6a-c). As shown in Fig. 6d,e,g-j, some CO_2 (C_2H_2) molecules are parallelly adsorbed on channel surfaces through $\text{C}_{\text{CO}_2}\text{-O}_{\text{Carbonyl}}$ ($\text{C-H}\cdots\text{O}_{\text{Carbonyl}}$ hydrogen bonds) interactions, and the remaining molecules interact with other framework atoms and adsorbed CO_2 (C_2H_2) molecules. The $\text{O}_{\text{Carbonyl}}$ site plays a crucial role in the CO_2 (C_2H_2) adsorption in Bi-MOF-H, mirrored also by the obvious $g(r)$ peaks in Fig. 7a,b. While C_2H_4 is just adsorbed through weak non-Coulomb interactions (or vdW

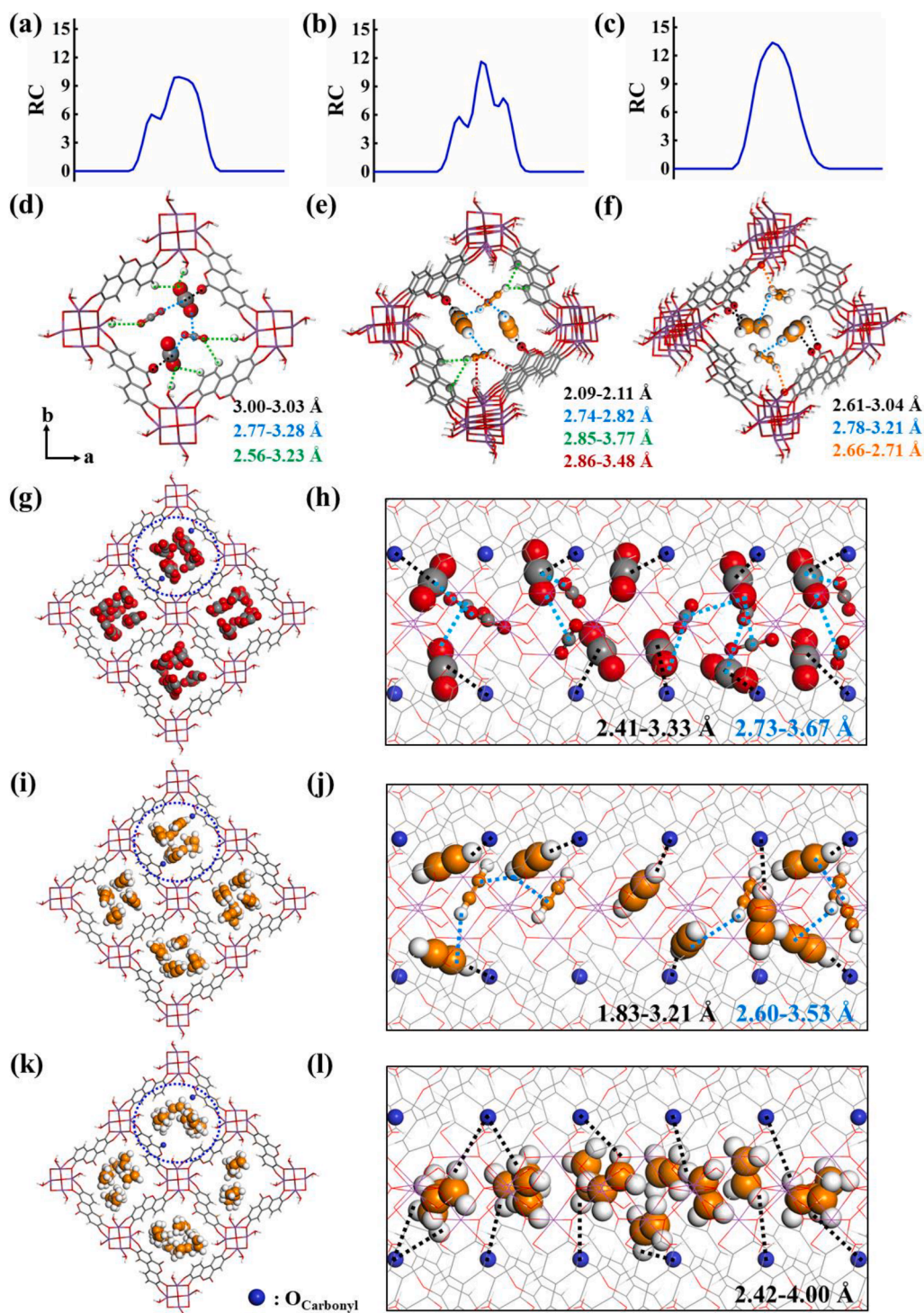


Fig. 6. The adsorption of CO_2 , C_2H_2 , and C_2H_4 in Bi-MOF-H at 298 K and 100 kPa. (a-c) Relative concentrations, (d-f) adsorption configurations, and (g-l) snapshots in channels from GCMC simulations (Top view: g, i, and k; Side view: h, j, and l).

interactions) without forming any specific adsorption configuration (Fig. 7c). To sum up, ligand substitution does not affect the packing pattern of CO_2 obviously but brings significant changes to $\text{C}_2\text{H}_2/\text{C}_2\text{H}_4$ adsorption, when compared with SU-101(Bi), in which $\text{C}_2\text{H}_2/\text{C}_2\text{H}_4$ gathers in channel centers accompanied by strong $g(r)$ peaks between $\text{C}_2\text{H}_2/\text{C}_2\text{H}_4$ and $\text{O}_{\text{Carbonyl}}$ atoms [27].

After functionalization (Figs. 8 and S16), CO_2 molecules were still adsorbed on channel surfaces, while the relative concentration exhibited two narrow peaks in channels along a -axis (Fig. 8a); C_2H_2 and C_2H_4

arranged orderly and nearly parallelly in two rows, also showing two narrow peaks (Fig. 8b,c). From Figs. 7d and S17a,d, the distances between CO_2 and $-\text{CHO}/-\text{NO}_2/-\text{COOH}$ are smaller than those at carbonyl, revealing the stronger CO_2 affinity of $-\text{CHO}/-\text{NO}_2/-\text{COOH}$. This is due to the high electronegativity as well as easier access of $\text{O}_{-\text{CHO}/-\text{NO}_2/-\text{COOH}}$ atoms. However, halogen sites show the weakened CO_2 affinity with larger distances towards CO_2 than those at carbonyl groups, owing to the smaller number of electrons in halogen atoms (Table 1).

C_2H_2 and C_2H_4 tend to bridge a $\text{O}_{\text{Carbonyl}}$ and its opposite functional

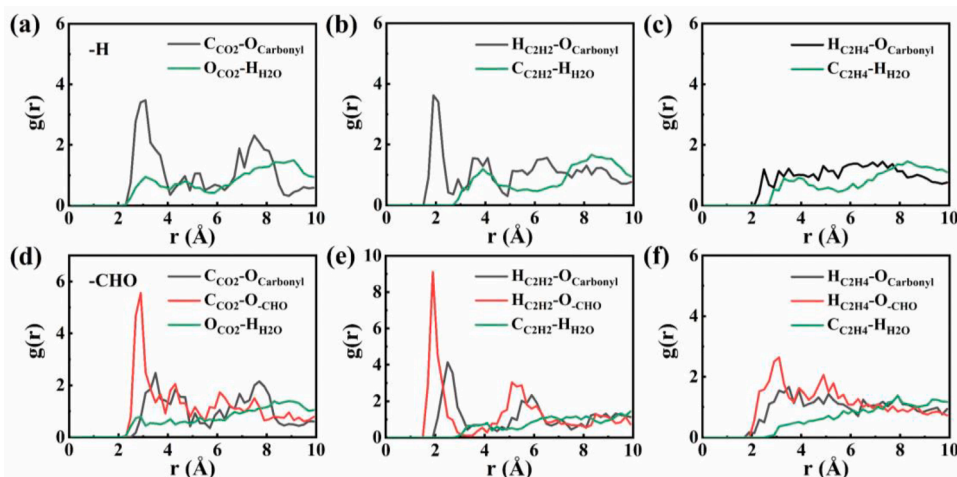


Fig. 7. Radial distribution functions (RDFs) of CO_2 , C_2H_2 , and C_2H_4 in (a-c) Bi-MOF-H and (d-f) Bi-MOF-CHO at 298 K and 100 kPa.

group through multiple hydrogen bonds shown in Fig. 8e,f. By considering snapshots and RDFs (Figs. 7e, 8, and S17), the C_2H_2 affinity of various bonding sites follows the same order as CO_2 adsorption: $-\text{CHO}/-\text{NO}_2/-\text{COOH} > \text{carbonyl} > \text{halogen sites}$, also attributed to the charge differences between functional-group electronegative atoms. For C_2H_4 adsorption, there is no $g(r)$ peak at carbonyl and functional groups for all Bi-MOFs, except for a weak $g(r)$ peak at O_{CHO} site in Bi-MOF-CHO (Figs. 7f and S17). Because the distances between carbonyl and functional groups (i.e., $d_{\text{X-O}_3/\text{O}_4} \geq 7 \text{ \AA}$, Fig. S3) can better match the molecule size of linear C_2H_2 (5.7 Å, Table S1) to generate a multiple-site recognition, but not suitable for C_2H_4 due to the smaller molecule size (4.8 Å) in plane structure.

For the snapshots of $\text{CO}_2/\text{C}_2\text{H}_4$ (Fig. S18b-d), introducing $-\text{CHO}/-\text{NO}_2/-\text{COOH}$ largely enhances the competitive adsorption for CO_2 , while suppresses the C_2H_4 adsorption in same regions. This is significantly different from that in SU-101, in which CO_2 is adsorbed on channel surfaces but C_2H_4 accumulates at channel centers [27]. For $\text{C}_2\text{H}_2/\text{C}_2\text{H}_4$ separation (Fig. S19b-d), the most ordered arrangement of C_2H_2 molecules and the shorter $\text{C}_2\text{H}_2\text{-O}_{\text{Surface}}$ distances (1.7 ~ 3.0 Å) ensure the best $\text{C}_2\text{H}_2/\text{C}_2\text{H}_4$ separation performance of Bi-MOF-CHO. What's important, the efficient separation of Bi-MOF-CHO/ $-\text{NO}_2/-\text{COOH}$ for $\text{CO}_2/\text{C}_2\text{H}_4$ and $\text{C}_2\text{H}_2/\text{C}_2\text{H}_4$ successfully verifies the prediction of divergent R_D values in Fig. 2. To sum up, Bi-MOF-CHO/ $-\text{NO}_2/-\text{COOH}$ can effectively purify C_2H_4 from C_2H_2 and CO_2 through one adsorbent, with Bi-MOF-CHO the most preferred.

3.5. Mechanisms in adsorption and separation processes

DFT calculations were performed to understand the influence of functional groups on the adsorption and separation properties of Bi-MOFs. In Bi-MOF-CHO/ $-\text{COOH}/-\text{NO}_2$ (Fig. 9b-d), the high electronegativity of surface O atoms ($-0.44e \sim -0.58e$) and ultramicroporous channel sizes facilitate multiple strong CO_2 -framework interactions and $\text{CO}_2\text{-CO}_2$ interactions; besides, the suitable distances between carbonyl and $-\text{CHO}/-\text{COOH}/-\text{NO}_2$ (i.e., $d_{\text{X-O}_2/\text{O}_3} = 5.14 \sim 5.30/7.00 \sim 7.03 \text{ \AA}$, Fig. S3) guarantee sufficient free space to adsorb CO_2 molecules for each $\text{O}_{\text{Carbonyl}}/\text{O}_{\text{Functional}}$ atom. All of these factors result in high CO_2 adsorption energy (59.2 ~ 66.4 kJ/mol) and the increased CO_2 uptakes with pressure (Fig. 3c) in Bi-MOF-CHO/ $-\text{COOH}/-\text{NO}_2$. In contrast, the low charge of $-\text{Cl}/-\text{Br}/-\text{I}$ ($-0.03e \sim -0.10e$) and small distances to O2 atoms (4.27 ~ 4.56 Å, Fig. S3) force CO_2 adsorbed with the $\text{O}_{\text{Carbonyl}} \cdots \text{CO}_2 \cdots \text{halogen}$ configuration, resulting in lower $\Delta E_{\text{ads}}(\text{CO}_2)$ of 47.9 ~ 53.7 kJ/mol (Fig. 9f-h); -F site shows the smallest $\Delta E_{\text{ads}}(\text{CO}_2)$ of 43.1 kJ/mol. For C_2H_2 adsorption, the $\text{O}_{\text{Carbonyl}} \cdots \text{H-C}\equiv\text{C-H} \cdots \text{X}_{\text{Functional}}$ configuration offsets the negative effect of pore size limitation,

predicting the moderate enhancement of C_2H_2 adsorption in Bi-MOFs except for Bi-MOF-CHO at low pressures (Fig. 3b).

Considering the $R_D(\text{C}_2\text{H}_4)$ values larger than $R_D(\text{C}_2\text{H}_2/\text{CO}_2)$ in Bi-MOF-CHO/ $-\text{COOH}/-\text{NO}_2$ (Fig. 2), we further analyzed the interactions between gases and Bi-MOFs shown in Fig. S20. Coulomb interaction of gas-framework plays a major role in CO_2 and C_2H_2 adsorption in Bi-MOF-CHO/ $-\text{COOH}/-\text{NO}_2$, owing to the stable adsorption configurations formed at surface functional groups. However, C_2H_4 adsorption is mainly dependent on non-Coulomb interaction (Fig. S20c), explaining almost no $g(r)$ peak during C_2H_4 adsorption and minor differences in C_2H_4 uptakes of functionalized Bi-MOFs (Fig. 3a); similar phenomenon also happens in CH_4 adsorption using MOF adsorbents [57,84]. Moreover, ignoring Coulomb interaction of gas-framework would lead to a dramatic decrease of the $\text{CO}_2/\text{C}_2\text{H}_2$ selectivity (<2.5) and even reverse the $\text{CO}_2/\text{C}_2\text{H}_4$ and $\text{C}_2\text{H}_2/\text{C}_2\text{H}_4$ separation (Fig. S20d-f), showing the importance of Coulomb interaction. In conclusion, introducing $-\text{CHO}/-\text{COOH}/-\text{NO}_2$ in Bi-MOFs can greatly facilitate the selective capture of CO_2 and C_2H_2 from $\text{C}_2\text{H}_4/\text{C}_2\text{H}_2/\text{CO}_2$ mixtures through precisely regulating the channel size and surface structure/electronegativity, thus realizing one-step C_2H_4 purification from ternary mixtures successfully.

4. Conclusion

In summary, Bi-MOFs modified with $-\text{CHO}$, $-\text{COOH}$, $-\text{NO}_2$, $-\text{F}$, $-\text{Cl}$, $-\text{Br}$, and $-\text{I}$ have been evaluated for $\text{CO}_2/\text{C}_2\text{H}_4$, $\text{C}_2\text{H}_2/\text{C}_2\text{H}_4$, and $\text{CO}_2/\text{C}_2\text{H}_2$ separations by GCMC and DFT. These Bi-MOFs exhibit good thermodynamic and thermal stability, and realize precise regulation of channel sizes and surface structures/electronegativity through functional groups. Among them, introducing $-\text{CHO}$, $-\text{COOH}$, and $-\text{NO}_2$ can enlarge the difference of adsorption amounts between CO_2 , C_2H_2 , and C_2H_4 , i.e., (1) a large enhancement for CO_2 owing to multiple and strong CO_2 -framework interactions and $\text{CO}_2\text{-CO}_2$ interactions; (2) moderate enhancement for C_2H_2 due to optimal channel structure and rich O sites; (3) negligible influence on C_2H_4 adsorption, in which non-Coulomb interaction of C_2H_4 -framework dominates. Thus, Bi-MOF-CHO/ $-\text{COOH}/-\text{NO}_2$ realizes efficient separation for $\text{CO}_2/\text{C}_2\text{H}_4$, $\text{C}_2\text{H}_2/\text{C}_2\text{H}_4$, and $\text{CO}_2/\text{C}_2\text{H}_2$ and, among them, Bi-MOF-CHO possesses the highest selectivity of 58.6, and 11.8, and 7.7 under 50/50 and 64.5, 11.5, and 21.5 under 1/99 at 298 K and 100 kPa, indicating its potential application in one-step C_2H_4 purification. Breakthrough simulations confirm the excellent one-step C_2H_4 purification performance of Bi-MOF-CHO, and the productivities of polymer grade C_2H_4 (>99.996%) for 1/1/98 and 1/9/90 $\text{C}_2\text{H}_2/\text{CO}_2/\text{C}_2\text{H}_4$ mixtures are 6.1 mol/kg (400.41 cm^3/cm^3) and 5.2 mol/kg (341.33 cm^3/cm^3), respectively. This work emphasizes the importance of precise channel-structure and surface-chemistry

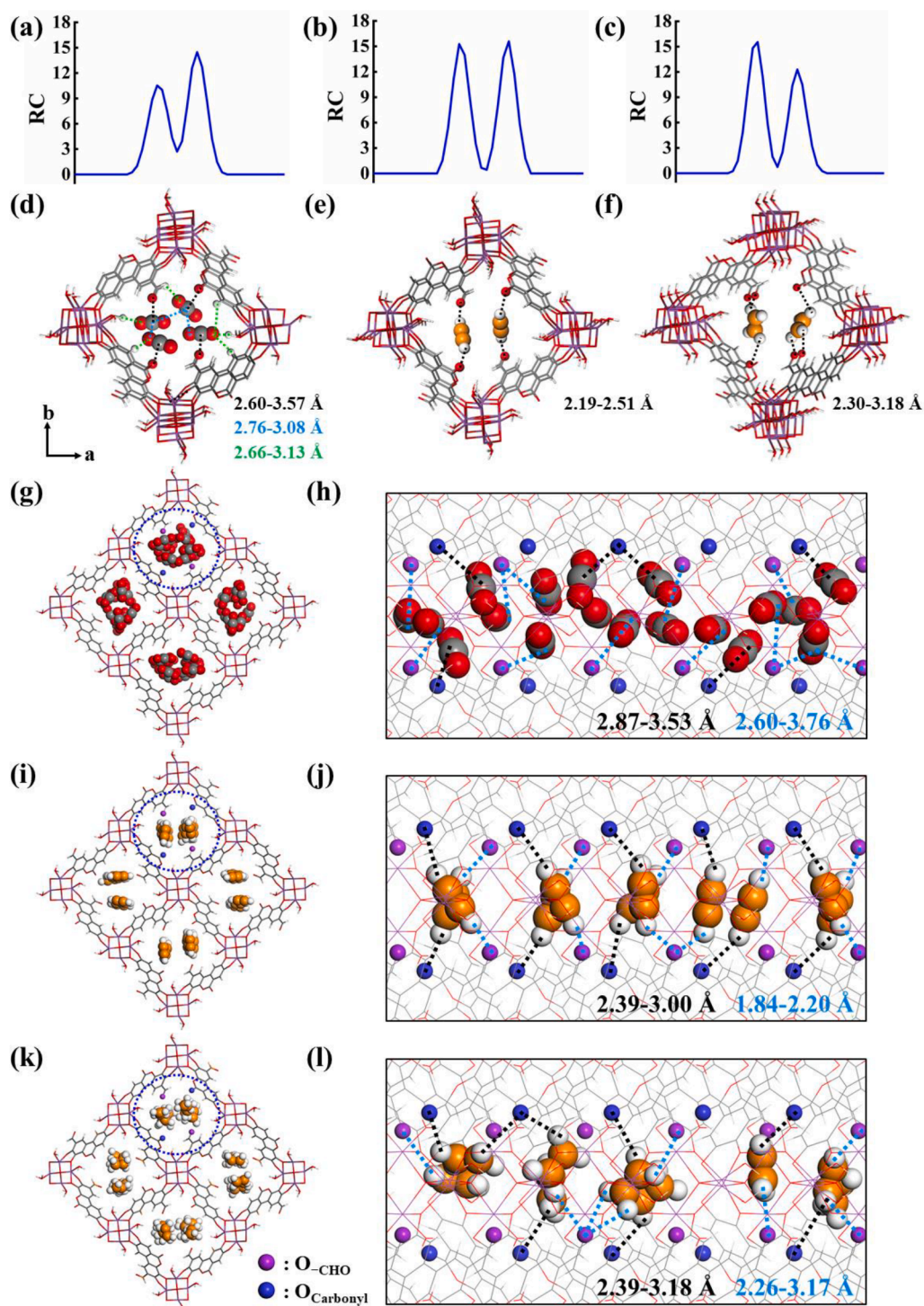


Fig. 8. The adsorption of CO_2 , C_2H_2 , and C_2H_4 in Bi-MOF-CHO at 298 K and 100 kPa. (a-c) Relative concentrations, (d-f) adsorption configurations, and (g-l) snapshots in channels from GCMC simulations (Top view: g, i, and k; Side view: h, j, and l).

regulation in Bi-MOFs for separating $\text{C}_2\text{H}_4/\text{C}_2\text{H}_2/\text{CO}_2$ mixtures, which will guide the development of multifunctional adsorbents for one-step C_2H_4 purification.

CRediT authorship contribution statement

Chunlian Hao: Investigation, Methodology, Writing – original draft. **Zhencui Ge:** Software, Writing – original draft. **Rajamani Krishna:** Methodology, Formal analysis, Writing – review & editing. **Hao Ren:** Formal analysis, Methodology, Funding acquisition. **Houyu Zhu:**

Methodology, Data curation. **Yuhua Chi:** Methodology, Data curation. **Wen Zhao:** Supervision, Data curation. **Xiuping Liu:** Writing – review & editing. **Wenyue Guo:** Resources, Conceptualization, Funding acquisition, Supervision, Writing – review & editing.

Declaration of Competing Interest

The authors declare that they have no known competing financial interests or personal relationships that could have appeared to influence the work reported in this paper.

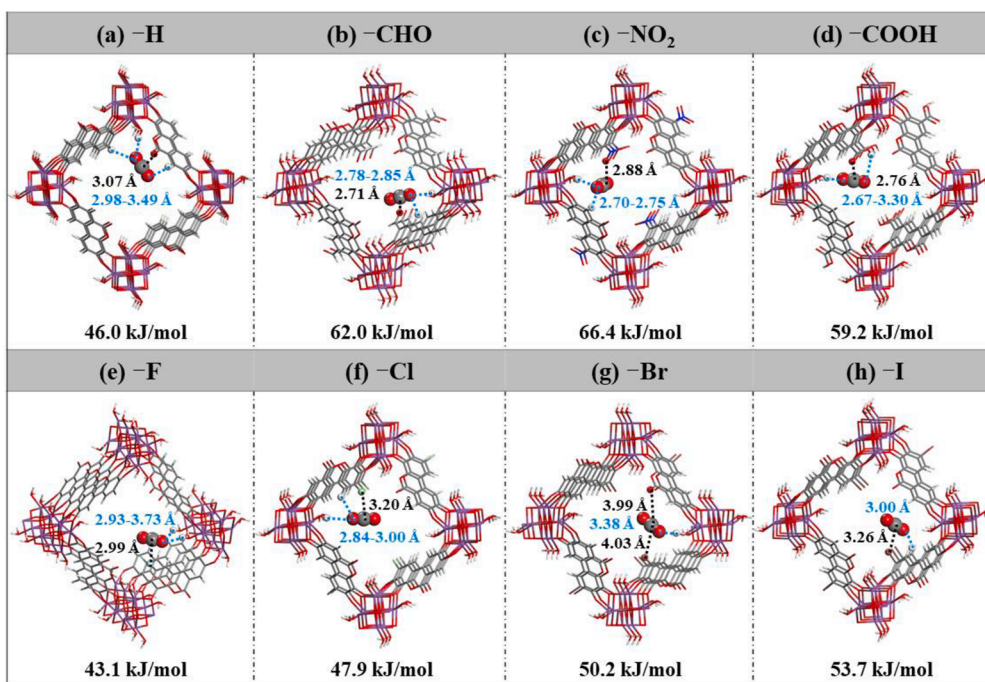


Fig. 9. DFT-optimized adsorption configurations and corresponding energies of a single CO₂ molecule in the channels of Bi-MOF materials.

Data availability

No data was used for the research described in the article.

Acknowledgments

This work was financially supported by the National Key Research and Development Program of China (2019YFA0708703), Taishan Scholars Program of Shandong Province (tsqn201909071), Natural Science Foundation of Shandong Province (ZR2020QB032), and Fundamental Research Funds for the Central Universities (19CX05001A and 20CX05010A).

Appendix A. Supplementary data

Supplementary data to this article can be found online at <https://doi.org/10.1016/j.cej.2023.144533>.

References

- [1] C. Choi, S. Kwon, T. Cheng, M. Xu, P. Tieu, C. Lee, J. Cai, H.M. Lee, X. Pan, X. Duan, W.A. Goddard, Y. Huang, Highly active and stable stepped Cu surface for enhanced electrochemical CO₂ reduction to C₂H₄, *Nat. Catal.* 3 (10) (2020) 804–812.
- [2] Ethylene—Global Market Trajectory and Analytics, Research and Markets (2020) https://www.researchandmarkets.com/reports/354876/ethylene_global_market_trajectory_and_analytics.
- [3] S. Nakanowatari, T.N. Nguyen, H. Chikuma, A. Fujiwara, K. Seenivasan, A. Thakur, L. Takahashi, K. Takahashi, T. Taniike, Extraction of catalyst design heuristics from random catalyst dataset and their utilization in catalyst development for oxidative coupling of methane, *ChemCatChem* 13 (14) (2021) 3262–3269.
- [4] X. Zhang, H. Cui, R.B. Lin, R. Krishna, Z.Y. Zhang, T. Liu, B. Liang, B. Chen, Realization of ethylene production from its quaternary mixture through metal-organic framework materials, *ACS Appl. Mater. Interfaces* 13 (19) (2021) 22514–22520.
- [5] I.v. Zandvoort, E.-J. Ras, R.d. Graaf, R. Krishna, Using transient breakthrough experiments for screening of adsorbents for separation of C₂H₄/CO₂ mixtures, *Sep. Purif. Technol.* 241 (2020), 116706.
- [6] Y.-M. Gu, H.-F. Qi, T.-T. Sun, X.-W. Liu, S. Qadir, T.-J. Sun, D.-F. Li, S.-S. Zhao, D. Fairen-Jimenez, S.-D. Wang, Insights into the ultra-high volumetric capacity in a robust metal-organic framework for efficient C₂H₂/CO₂ separation, *Chem. Mater.* 34 (6) (2022) 2708–2716.
- [7] W. Gong, H. Cui, Y. Xie, Y. Li, X. Tang, Y. Liu, Y. Cui, B. Chen, Efficient C₂H₂/CO₂ separation in ultramicroporous metal-organic frameworks with record C₂H₂ storage density, *J. Am. Chem. Soc.* 143 (36) (2021) 14869–14876.
- [8] G.D. Wang, Y.Z. Li, W.J. Shi, L. Hou, Y.Y. Wang, Z. Zhu, One-step C₂H₄ purification from ternary C₂H₆/C₂H₄/C₂H₂ mixtures by a robust metal-organic framework with customized pore environment, *Angew. Chem. Int. Ed.* 61 (28) (2022) e202205427.
- [9] L. Wang, W. Sun, Y. Zhang, N. Xu, R. Krishna, J. Hu, Y. Jiang, Y. He, H. Xing, Interpenetration symmetry control within ultramicroporous robust boron cluster hybrid MOFs for benchmark purification of acetylene from carbon dioxide, *Angew. Chem. Int. Ed.* 60 (42) (2021) 22865–22870.
- [10] X. Liu, P. Zhang, H. Xiong, Y. Zhang, K. Wu, J. Liu, R. Krishna, J. Chen, S. Chen, Z. Zeng, S. Deng, J. Wang, Engineering pore environments of sulfate-pillared metal-organic framework for efficient C₂H₂/CO₂ separation with record selectivity, *Adv. Mater.* 35 (20) (2023) 2210415.
- [11] T. He, Y. Xiao, Q. Zhao, M. Zhou, G. He, Ultramicroporous metal-organic framework Qc-5-Cu for highly selective adsorption of CO₂ from C₂H₄ stream, *Ind. Eng. Chem. Res.* 59 (7) (2020) 3153–3161.
- [12] K.J. Chen, D.G. Madden, S. Mukherjee, T. Pham, M.J. Zaworotko, Synergistic sorbent separation for one-step ethylene purification from a four-component mixture, *Science* 366 (6462) (2019) 241–246.
- [13] J.R. Li, R.J. Kuppler, H.C. Zhou, Selective gas adsorption and separation in metal-organic frameworks, *Chem. Soc. Rev.* 38 (5) (2009) 1477–1504.
- [14] G.-D. Wang, H.-H. Wang, W.-J. Shi, L. Hou, Y.-Y. Wang, Z. Zhu, A highly stable MOF with F and N accessible sites for efficient capture and separation of acetylene from ternary mixtures, *J. Mater. Chem. A* 9 (43) (2021) 24495–24502.
- [15] H. Wang, Y. Liu, J. Li, Designer metal-organic frameworks for size-exclusion-based hydrocarbon separations: progress and challenges, *Adv. Mater.* 32 (44) (2020) 2002603.
- [16] F. Jin, E. Lin, T. Wang, S. Geng, T. Wang, W. Liu, F. Xiong, Z. Wang, Y. Chen, P. Cheng, Z. Zhang, Bottom-up synthesis of 8-connected three-dimensional covalent organic frameworks for highly efficient ethylene/ethane separation, *J. Am. Chem. Soc.* 144 (12) (2022) 5643–5652.
- [17] S. Chaemchuen, N.A. Kabir, K. Zhou, F. Verpoort, Metal-organic frameworks for upgrading biogas via CO₂ adsorption to biogas green energy, *Chem. Soc. Rev.* 42 (24) (2013) 9304–9332.
- [18] Q. Yang, D. Liu, C. Zhong, J.R. Li, Development of computational methodologies for metal-organic frameworks and their application in gas separations, *Chem. Rev.* 113 (10) (2013) 8261–8323.
- [19] H. Li, K. Wang, Y. Sun, C.T. Lollar, J. Li, H.-C. Zhou, Recent advances in gas storage and separation using metal-organic frameworks, *Mater. Today* 21 (2) (2018) 108–121.
- [20] Y. Wu, B.M. Weckhuysen, Separation and purification of hydrocarbons with porous materials, *Angew. Chem. Int. Ed.* 60 (35) (2021) 18930–18949.
- [21] Z. Xu, X. Xiong, J. Xiong, R. Krishna, L. Li, Y. Fan, F. Luo, B. Chen, A robust Thazole framework for highly efficient purification of C₂H₄ from a C₂H₄/C₂H₂/C₂H₆ mixture, *Nat. Commun.* 11 (1) (2020) 3163.
- [22] H.G. Hao, Y.F. Zhao, D.M. Chen, J.M. Yu, K. Tan, S. Ma, Y. Chabal, Z.M. Zhang, J. M. Dou, Z.H. Xiao, G. Day, H.C. Zhou, T.B. Lu, Simultaneous trapping of C₂H₂ and C₂H₆ from a ternary mixture of C₂H₂/C₂H₄/C₂H₆ in a robust metal-organic framework for the purification of C₂H₄, *Angew. Chem. Int. Ed.* 57 (49) (2018) 16067–16071.
- [23] S. Mukherjee, S. Chen, A.A. Bezrukov, M. Mostrom, V.V. Tersikh, D. Franz, S. Q. Wang, A. Kumar, M. Chen, B. Space, Ultramicropore engineering by dehydration

- to enable molecular sieving of H₂ by calcium trimesate, *Angew. Chem. Int. Ed.* 59 (37) (2020) 16188–16194.
- [24] S. Mukherjee, N. Kumar, A.A. Bezrukov, K. Tan, T. Pham, K.A. Forrest, K. A. Oyekan, O.T. Qazvini, D.G. Madden, B. Space, M.J. Zaworotko, Amino-functionalised hybrid ultramicroporous materials that enable single-step ethylene purification from a ternary mixture, *Angew. Chem. Int. Ed.* 60 (19) (2021) 10902–10909.
- [25] J.W. Cao, S. Mukherjee, T. Pham, Y. Wang, T. Wang, T. Zhang, X. Jiang, H.J. Tang, K.A. Forrest, B. Space, M.J. Zaworotko, K.J. Chen, One-step ethylene production from a four-component gas mixture by a single physisorbent, *Nat. Commun.* 12 (1) (2021) 6507.
- [26] Y. Jiang, Y. Hu, B. Luan, L. Wang, R. Krishna, H. Ni, X. Hu, Y. Zhang, Benchmark single-step ethylene purification from ternary mixtures by a customized fluorinated anion-embedded MOF, *Nat. Commun.* 14 (1) (2023) 401.
- [27] C. Hao, H. Ren, H. Zhu, Y. Chi, W. Zhao, X. Liu, W. Guo, CO₂-favored metal-organic frameworks SU-101(M) (M = Bi, In, Ga, and Al) with inverse and high selectivity of CO₂ from C₂H₂ and C₂H₄, *Sep. Purif. Technol.* 290 (2022), 120804.
- [28] Q.-X. Wang, G. Li, Bi(III) MOFs: syntheses, structures and applications, *Inorg. Chem. Front.* 8 (3) (2021) 572–589.
- [29] Y. Sano, H. Satoh, M. Chiba, M. Okamoto, K. Serizawa, H. Nakashima, K. Omae, Oral toxicity of bismuth in rat: single and 28-day repeated administration studies, *J. Occup. Health* 47 (4) (2005) 293–298.
- [30] E.S. Grape, J.G. Flores, T. Hidalgo, E. Martinez-Ahumada, A. Gutierrez-Alejandre, A. Hautier, D.R. Williams, M. O’Keeffe, L. Ohrstrom, T. Willhammar, P. Horcajada, I.A. Ibarra, A.K. Inge, A robust and biocompatible bismuth ellagate MOF synthesized under green ambient conditions, *J. Am. Chem. Soc.* 142 (39) (2020) 16795–16804.
- [31] T.F. Willems, C.H. Rycroft, M. Kazi, J.C. Meza, M. Haranczyk, Algorithms and tools for high-throughput geometry-based analysis of crystalline porous materials, *Micropor. Mesopor. Mater.* 149 (1) (2012) 134–141.
- [32] R.L. Martin, B. Smit, M. Haranczyk, Addressing challenges of identifying geometrically diverse sets of crystalline porous materials, *J. Chem. Inf. Model.* 52 (2) (2012) 308–318.
- [33] B. Delley, From molecules to solids with the DMOL³ approach, *J. Chem. Phys.* 113 (18) (2000) 7756–7764.
- [34] A. Tkatchenko, M. Scheffler, Accurate molecular van der Waals interactions from ground-state electron density and free-atom reference data, *Phys. Rev. Lett.* 102 (7) (2009), 073005.
- [35] G. Kresse, J. Furthmüller, Efficiency of Ab-initio total energy calculations for metals and semiconductors using a plane-wave basis set, *Comput. Mater. Sci.* 6 (1996) 15–50.
- [36] G. Kresse, J. Furthmüller, Efficient iterative schemes for ab initio total-energy calculations using a plane-wave basis set, *Phys. Rev. B* 54 (1996) 11169–11186.
- [37] G. Kresse, J. Hafner, Ab initio molecular dynamics for liquid metals, *Phys. Rev. B* 47 (1) (1993) 558–561.
- [38] E. Perim, R. Paupitz, P. Autreto, D. Galvao, Inorganic graphenylene: A porous two-dimensional material with tunable band gap, *J. Phys. Chem. C* 118 (41) (2014) 23670–23674.
- [39] L. Zhao, S. Guo, H. Liu, H. Zhu, S. Yuan, W. Guo, Density functional study of hydrogen evolution on cobalt-embedded carbon nanotubes: effects of doping and surface curvature, *ACS Appl. Nano Mater.* 1 (11) (2018) 6258–6268.
- [40] J.-C. Zheng, H.-Q. Wang, A.T.S. Wee, C.H.A. Huan, Trends in bonding configuration at SiC/III-V semiconductor interfaces, *Appl. Phys. Lett.* 79 (11) (2001) 1643–1645.
- [41] P. Jund, R. Vienneis, C. Colinet, G. Hug, M. Fevre, J.C. Tedenac, Lattice stability and formation energies of intrinsic defects in Mg₂Si and Mg₂Ge via first principles simulations, *J. Phys.: Condens. Matter* 25 (3) (2013), 035403.
- [42] W.G. Hoover, Canonical dynamics: equilibrium phase-space distributions, *Phys. Rev. A* 31 (3) (1985) 1695–1697.
- [43] A. Gupta, S. Chempath, M.J. Sanborn, L.A. Clark, R.Q. Snurr, Object-oriented programming paradigms for molecular modeling, *Mol. Simulat.* 29 (1) (2003) 29–46.
- [44] J.J. Potoff, J.I. Siepmann, Vapor-liquid equilibria of mixtures containing alkanes, carbon dioxide, and nitrogen, *AIChE J.* 47 (7) (2001) 1676–1682.
- [45] S.L. Weitz, J.J. Potoff, Effect of quadrupole moment on the phase behavior of binary mixtures containing ethene, *Fluid Phase Equilib.* 234 (1–2) (2005) 144–150.
- [46] M. Fischer, F. Hoffmann, M. Fröba, New microporous materials for acetylene storage and C₂H₂/CO₂ separation: Insights from molecular simulations, *ChemPhysChem* 11 (10) (2010) 2220–2229.
- [47] A.K. Rappé, C.J. Casewit, K. Colwell, W.A. Goddard III, W.M. Skiff, UFF, a full periodic table force field for molecular mechanics and molecular dynamics simulations, *J. Am. Chem. Soc.* 114 (25) (1992) 10024–10035.
- [48] S.L. Mayo, B.D. Olafson, W.A. Goddard, DREIDING: a generic force field for molecular simulations, *J. Phys. Chem.* 94 (26) (1990) 8897–8909.
- [49] C. Jiang, C. Hao, X. Wang, H. Liu, X. Wei, H. Xu, Z. Wang, Y. Ouyang, W. Guo, F. Dai, D. Sun, Constructing C₂H₂ anchoring traps within MOF interpenetration nets as C₂H₂/CO₂ and C₂H₂/C₂H₄ bifunctional separator, *Chem. Eng. J.* 453 (2023), 139713.
- [50] X. Liu, W. Fan, M. Zhang, G. Li, H. Liu, D. Sun, L. Zhao, H. Zhu, W. Guo, Enhancing light hydrocarbon storage and separation through introducing Lewis basic nitrogen sites within a carboxylate-decorated copper-organic framework, *Mater. Chem. Front.* 2 (6) (2018) 1146–1154.
- [51] J. Pang, F. Jiang, M. Wu, C. Liu, K. Su, W. Lu, D. Yuan, M. Hong, A porous metal-organic framework with ultrahigh acetylene uptake capacity under ambient conditions, *Nat. Commun.* 6 (1) (2015) 7575.
- [52] W. Gong, Y. Xie, T.D. Pham, S. Shetty, F.A. Son, K.B. Idrees, Z. Chen, H. Xie, Y. Liu, R.Q. Snurr, B. Chen, B. Alameddine, Y. Cui, O.K. Farha, Creating optimal pockets in a clathrocholate-based metal-organic framework for gas adsorption and separation: experimental and computational studies, *J. Am. Chem. Soc.* 144 (8) (2022) 3737–3745.
- [53] B. Han, A. Chakraborty, Tailoring zirconium-based metal organic frameworks for enhancing hydrophilic/hydrophobic characteristics: simulation and experimental investigation, *J. Mol. Liq.* 341 (2021), 117381.
- [54] R. Huang, M.R. Hill, R. Babarao, N.V. Medhekar, CO₂ adsorption in azobenzene functionalized stimuli responsive metal-organic frameworks, *J. Phys. Chem. C* 120 (30) (2016) 16658–16667.
- [55] W. Wei, K. Zhang, Z. Qiao, J. Jiang, Functional UiO-66 for the removal of sulfur-containing compounds in gas and liquid mixtures: a molecular simulation study, *Chem. Eng. J.* 356 (2019) 737–745.
- [56] C. Gu, Y. Liu, W. Wang, J. Liu, J. Hu, Effects of functional groups for CO₂ capture using metal organic frameworks, *Front. Chem. Sci. Eng.* 15 (2) (2021) 437–449.
- [57] C. Gu, J. Liu, J. Hu, D. Wu, Metal-organic frameworks chelated by zinc fluorides for ultra-high affinity to acetylene during C₂/C₁ separations, *Fuel* 266 (2020), 117037.
- [58] C. Gu, J. Liu, J. Hu, D. Wu, Highly selective separations of C₂H₂/C₂H₄ and C₂H₂/C₂H₆ in metal-organic frameworks via pore environment design, *Ind. Eng. Chem. Res.* 58 (43) (2019) 19946–19957.
- [59] D. Zhang, X. Jing, D.S. Sholl, S.B. Sinnott, Molecular simulation of capture of sulfur-containing gases by porous aromatic frameworks, *J. Phys. Chem. C* 122 (32) (2018) 18456–18467.
- [60] S. Chen, X. Li, J. Duan, Y. Fu, Z. Wang, M. Zhu, N. Li, Investigation of highly efficient adsorbent based on Ni-MOF-74 in the separation of CO₂ from natural gas, *Chem. Eng. J.* 419 (2021), 129653.
- [61] P.G. Boyd, A. Chidambaram, E. Garcia-Diez, C.P. Ireland, T.D. Daff, R. Bounds, A. Gladysiak, P. Schouwink, S.M. Moosavi, M.M. Maroto-Valer, J.A. Reimer, J.A. R. Navarro, T.K. Woo, S. Garcia, K.C. Stylianou, B. Smit, Data-driven design of metal-organic frameworks for wet fuel gas CO₂ capture, *Nature* 576 (7786) (2019) 253–256.
- [62] S. Lee, B. Kim, H. Cho, H. Lee, S.Y. Lee, E.S. Cho, J. Kim, Computational screening of yrrillions of metal-organic frameworks for high-performance methane storage, *ACS Appl. Mater. Interfaces* 13 (20) (2021) 23647–23654.
- [63] S.-Y. Kim, S.-I. Kim, Y.-S. Bae, Machine-learning-based prediction of methane adsorption isotherms at varied temperatures for experimental adsorbents, *J. Phys. Chem. C* 124 (36) (2020) 19538–19547.
- [64] G.D. Degaga, R. Pandey, C. Gupta, L. Bharadwaj, Tailoring of the electronic property of Zn-BTC metal-organic framework via ligand functionalization: an ab initio investigation, *RSC Adv.* 9 (25) (2019) 14260–14267.
- [65] P. Suksaengrat, V. Amornkitbamrung, P. Srepusharwoot, Enhancements of hydrogen adsorption energy in M-MOF-525 (M = Ti, V, Zr and Hf): A DFT study, *Chin. J. Phys.* 64 (2020) 326–332.
- [66] G. Liu, L. Ma, S. Xiang, Chemistry and Chemical property data manual: Inorganic volume (Chinese Edition), Chemical Industry Press, Beijing, 2013.
- [67] J. Standing, B.W. Ashton, The effect of radiolytic oxidation by carbon dioxide on the porosity of graphite, *Carbon* 3 (2) (1965) 157–165.
- [68] S. Chand Pal, R. Krishna, M.C. Das, Highly scalable acid-base resistant Cu-Prussian blue metal-organic framework for C₂H₂/C₂H₄, biogas, and flue gas separations, *Chem. Eng. J.* 460 (2023), 141795.
- [69] W. Fan, S.B. Peh, Z. Zhang, H. Yuan, Z. Yang, Y. Wang, K. Chai, D. Sun, D. Zhao, Tetrazole-functionalized zirconium metal-organic cages for efficient C₂H₂/C₂H₄ and C₂H₂/CO₂ separations, *Angew. Chem. Int. Ed.* 60 (32) (2021) 17338–17343.
- [70] O.T. Qazvini, R. Babarao, S.G. Telfer, Selective capture of carbon dioxide from hydrocarbons using a metal-organic framework, *Nat. Commun.* 12 (1) (2021) 197.
- [71] S. Horike, K. Kishida, Y. Watanabe, Y. Inubushi, D. Umeyama, M. Sugimoto, T. Fukushima, M. Inukai, S. Kitagawa, Dense coordination network capable of selective CO₂ capture from C₁ and C₂ hydrocarbons, *J. Am. Chem. Soc.* 134 (24) (2012) 9852–9855.
- [72] S. Yang, A.J. Ramirez-Cuesta, R. Newby, V. Garcia-Sakai, P. Manuel, S.K. Callear, S. I. Campbell, C.C. Tang, M. Schroder, Supramolecular binding and separation of hydrocarbons within a functionalized porous metal-organic framework, *Nat. Chem.* 7 (2) (2015) 121–129.
- [73] X. Cui, K. Chen, H. Xing, Q. Yang, R. Krishna, Z. Bao, H. Wu, W. Zhou, X. Dong, Y. Han, B. Li, Q. Ren, M.J. Zaworotko, B. Chen, Pore chemistry and size control in hybrid porous materials for acetylene capture from ethylene, *Science* 353 (6295) (2016) 141–144.
- [74] E.D. Bloch, W.L. Queen, R. Krishna, J.M. Zadrozny, C.M. Brown, J.R. Long, Hydrocarbon separations in a metal-organic framework with open iron(II) coordination sites, *Science* 335 (6076) (2012) 1606–1610.
- [75] M.O. Barsukova, K.A. Kovalenko, A.S. Nizovtsev, A.A. Sapiyanik, D.G. Samsonenko, D.N. Dybtsev, V.P. Fedin, Isomeric scandium-organic frameworks with high hydrolytic stability and selective adsorption of acetylene, *Inorg. Chem.* 60 (5) (2021) 2996–3005.
- [76] L. Yang, A. Jin, L. Ge, X. Cui, H. Xing, A novel interpenetrated anion-pillared porous material with high water tolerance afforded efficient C₂H₂/C₂H₄ separation, *Chem. Commun.* 55 (34) (2019) 5001–5004.
- [77] T.L. Hu, H. Wang, B. Li, R. Krishna, H. Wu, W. Zhou, Y. Zhao, Y. Han, X. Wang, W. Zhu, Z. Yao, S. Xiang, B. Chen, Microporous metal-organic framework with dual functionalities for highly efficient removal of acetylene from ethylene/acetylene mixtures, *Nat. Commun.* 6 (2015) 7328.

- [78] Q. Zhang, S.-Q. Yang, L. Zhou, L. Yu, Z.-F. Li, Y.-J. Zhai, T.-L. Hu, Pore-space partition through an embedding metal-carboxylate chain-induced topology upgrade strategy for the separation of acetylene/ethylene, *Inorg. Chem.* 60 (24) (2021) 19328–19335.
- [79] H. Wang, X. Zeng, W. Wang, D. Cao, Selective capture of trace sulfur gas by porous covalent-organic materials, *Chem. Eng. Sci.* 135 (2015) 373–380.
- [80] Q. Dong, Y. Huang, K. Hyeon-Deuk, I.Y. Chang, J. Wan, C. Chen, J. Duan, W. Jin, S. Kitagawa, Shape- and size-dependent kinetic ethylene sieving from a ternary mixture by a trap-and-flow channel crystal, *Adv. Funct. Mater.* 32 (38) (2022) 2203745.
- [81] B.L. Farrell, V.O. Igenegbai, S. Linic, A viewpoint on direct methane conversion to ethane and ethylene using oxidative coupling on solid catalysts, *ACS Catal.* 6 (7) (2016) 4340–4346.
- [82] R. Krishna, Synergistic and antisnergistic intracrystalline diffusional influences on mixture separations in fixed-bed adsorbers, *Precis. Chem.* 1 (2) (2023) 83–93.
- [83] R. Krishna, Methodologies for evaluation of metal–organic frameworks in separation applications, *RSC Adv.* 5 (64) (2015) 52269–52295.
- [84] S. Zhou, M. Wang, S. Wei, Z. Wang, S. Liu, C.-M. Lawrence Wu, D. Sun, X. Lu, Precise regulation of CO₂ packing pattern in s-block metal doped single-layer covalent organic frameworks for high-performance CO₂ capture and separation, *Chem. Eng. J.* 441 (2022), 135903.

Supplementary Information

Fine-tuning channel structure and surface chemistry of stable bismuth-organic frameworks for efficient C₂H₄ purification through reversely trapping CO₂ and C₂H₂

Chunlian Hao^a, Zhencui Ge^b, Hao Ren^a, Houyu Zhu^a, Yuhua Chi^a, Wen Zhao^a, Xiuping Liu^c, Wenyue Guo^{a,*}

^a *School of Materials Science and Engineering, China University of Petroleum, Qingdao, Shandong 266580, People's Republic of China.*

^b *College of Science, China University of Petroleum, Qingdao, Shandong 266580, People's Republic of China.*

^c *School of Materials Science and Engineering, Linyi University, Linyi, Shandong 276000, People's Republic of China.*

*Corresponding authors: Wenyue Guo

E-mail address: wyguo@upc.edu.cn

Section S1 Molecular dynamics (MD) simulation details

MD simulations were performed to analyze the diffusion behavior between gases and functionalized Bi-MOFs, including mean square displacement (MSD) and diffusion coefficient (see Figs. S12 and S13). All simulations were carried out by BIOVIA Materials Studio software package. In the first step, the energy and geometry of the total systems of adsorbates and adsorbents obtained from GCMC calculation were optimized using the Forcite module. The UFF force field was applied for all optimization. Ewald and Atom-Based integration method were applied for modeling and calculation of the electrostatic and van der Waals energy potential at constant temperatures. In order to reach the equilibrium state, Canonical ensemble (NVT) was initially applied for 500 ps on systems. Micro-Canonical ensemble (NVE) was applied on systems for 5 ps to reach the equilibrium.

MSD is the deviation of a particle's position towards a referenced position over time, which can be calculated using the following equation:

$$MSD = \frac{1}{n} \sum_{n=1}^N [x_n(t) - x_n(0)]^2$$

where N is the number of particles to be averaged, $x_n(0)$ is the referenced position of each particle and $x_n(t)$ is the specific position of a particle at time t .

The diffusion coefficient can be calculated using the following equation:

$$D = \frac{1}{6N} \lim_{t \rightarrow \infty} \frac{d}{dt} \sum_{n=1}^N (x_n(t) - x_n(0))^2$$

Where $\frac{d}{dt}$ represents the slope of MSD curve.

Section S2 Transient breakthrough simulations

Transient breakthrough simulations were carried out for the same set of operating conditions as in the experimental data sets, using the methodology described in earlier publications [1-5]. To demonstrate the separation capabilities of Bi-MOF-CHO, Bi-MOF-NO₂, and Bi-MOF-COOH, we performed breakthrough simulations for 1/1/98 C₂H₂/CO₂/C₂H₄ and 1/9/90 C₂H₂/CO₂/C₂H₄ ternary mixtures at 298 K and $P_t = 10^5$ Pa total pressure. We considered the influence of intra-crystalline diffusion, and the intra-MOF diffusivities used for C₂H₂, CO₂, and C₂H₄ were determined from MD simulations (Fig. S13). The radius of the crystallites used in the simulations $r_c = 2$ nm.

Breakthrough simulations were performed with following parameters: the adsorber length, $L = 0.3$ m; the cross-sectional area, $A = 1$ m²; the interstitial gas velocity in the packed bed, $v = 0.1$ m/s; the voidage of the packed bed, $\varepsilon = 0.4$; the superficial gas velocity at the inlet to the packed bed, $u_0 = 0.04$ m/s; the volumetric flow rate of the gas mixture at the inlet, $Q_0 = 40$ L/s. The total volume of the packed bed is $V_{bed} = LA$. The volume of Bi-MOFs in the packed bed is $V_{ads} = LA(1-\varepsilon) = 0.18$ m³. The mass of Bi-MOFs in the packed bed is $m_{ads} = \rho LA(1-\varepsilon)$, where ρ is the crystal density of Bi-MOFs (see Table 1 in the main text).

The mixture adsorption equilibrium were determined using the Ideal Adsorbed Solution Theory (IAST) of Myers and Prausnitz [7]; the unary isotherm data used are based on molecular simulations (Fig. 3a-c in the main text).

The breakthrough data (Figs. S14, S15, and Fig. 5c,d in the main manuscript) are presented in terms of the dimensionless concentrations at the exit of the fixed bed,

c_i/c_{i0} , as function of the modified time parameter

$$\frac{(Q_0 = \text{flow rate L s}^{-1}) \times (\text{time in s})}{(\text{kg MOF packed in tube})} = \frac{Q_0 t}{m_{\text{ads}}} = \text{L kg}^{-1}.$$

The objective of the simulations is to demonstrate that Bi-MOFs are capable of one-step purification of C₂H₂/CO₂/C₂H₄ mixtures to produce C₂H₄ that fulfils the purity requirement of the feedstock to polymerization reactors. Industry demands that C₂H₂ be present in concentrations below 40 ppm; this translates to a C₂H₄ purity of >99.996% (polymer grade C₂H₄) [6]. Based on the breakthrough data, we can gain the productivities of polymer grade C₂H₄ by doing the calculations as shown in **Fig. S2-1**.

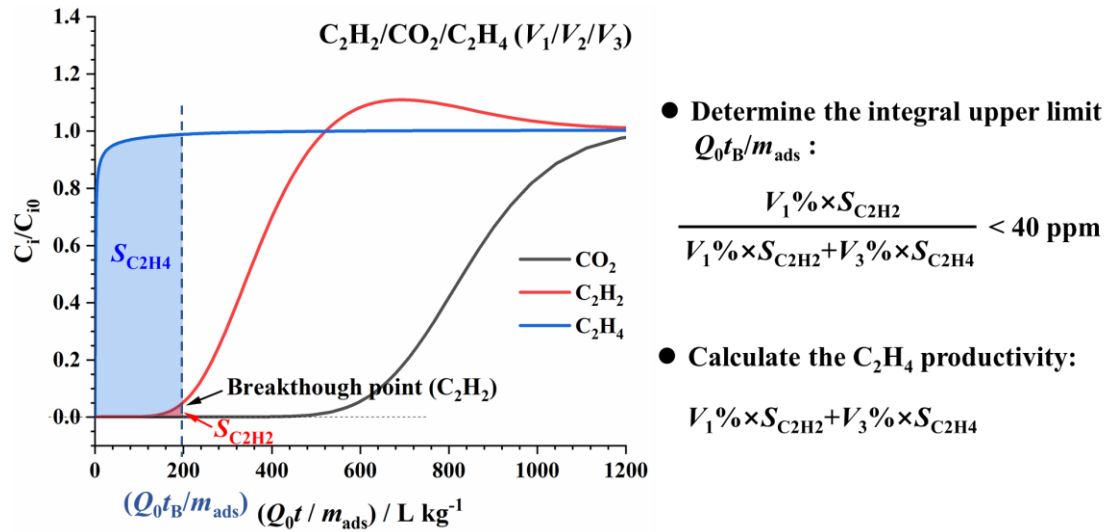


Fig. S2-1 Simulated breakthrough curves of a representative adsorbent for C₂H₂/CO₂/C₂H₄ (V₁/V₂/V₃) mixtures. S_{C₂H₂} (S_{C₂H₄}) represents the C₂H₂ (C₂H₄) amount in the outlet leaving fixed-bed adsorbers, which is the integral of C_i/C_{i0} between 0 and Q₀t_B/m_{ads}. The integral upper limit Q₀t_B/m_{ads} is determined by the condition of the C₂H₂ impurity below 40 ppm.

The calculated productivities of polymer grade C_2H_4 are listed in Tables S8 and S9. It is clear that the productivity of purified C_2H_4 is adversely influenced by intra-crystalline diffusion in all the three Bi-MOFs, which accounts for relatively flat breakthrough curves due to the slow diffusion within the channels. Considering the intra-crystalline diffusion, Bi-MOF-CHO is the best and excellent performing MOF, but the performance of both Bi-MOF- NO_2 and Bi-MOF-COOH are rather poor.

Section S3 Nomenclature

Latin alphabet

c_i	molar concentration of species i , mol m ⁻³
c_{i0}	molar concentration of species i in fluid mixture at inlet to adsorber, mol m ⁻³
D_i	Maxwell-Stefan diffusivity for molecule-wall interaction, m ² s ⁻¹
m_{ads}	mass of adsorbent packed in fixed bed, kg
L	length of packed bed adsorber, m
p_t	total system pressure, Pa
Q_0	volumetric flow rate of gas mixture entering fixed bed, m ³ s ⁻¹
r_c	radius of crystallite, m
t	time, s
u	superficial gas velocity in packed bed, m s ⁻¹
v	interstitial gas velocity in packed bed, m s ⁻¹

Greek alphabet

ε	voidage of packed bed, dimensionless
ρ	framework density, kg m ⁻³

Subscripts

i	referring to component i
t	referring to total mixture

Table S1 Physical properties of CO₂, C₂H₂, and C₂H₄ [8, 9].

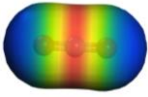
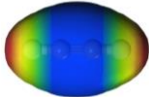
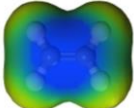
Molecules	CO ₂	C ₂ H ₂	C ₂ H ₄
Electrostatic potential			
Dimensions (Å ³)	3.18×3.38×5.36	3.32×3.34×5.70	3.28×4.18×4.84
Kinetic diameter (Å)	3.3	3.3	4.2
Quadrupole moment (×10 ²⁶ esu cm ²)	4.3	3.0	1.5
Polarisability (Å ³)	2.91	3.33~3.93	4.25
Boiling point (K)	194.7	189.4	169.5

Table S2 Crystal data and structure refinement for Bi-MOFs.

	Bi-MOF-H	Bi-MOF-NO ₂	Bi-MOF-CHO
Chemical formula	Bi ₂ O(H ₂ O) ₂ (C ₁₃ H ₄ O ₆)	Bi ₂ O(H ₂ O) ₂ (C ₁₃ H ₃ O ₈ N)	Bi ₂ O(H ₂ O) ₂ (C ₁₄ H ₄ O ₇)
Formula weight	726.194	771.196	754.204
Crystal system	Tetragonal	Tetragonal	Tetragonal
Space group	P42	P42	P42
<i>a</i> (Å)	19.2520	19.2444	19.2398
<i>b</i> (Å)	19.2520	19.2444	19.2398
<i>c</i> (Å)	5.10790	5.10796	5.10836
<i>α</i> (°)	90.0000	90.0000	90.0000
<i>β</i> (°)	90.0000	90.0000	90.0000
<i>γ</i> (°)	90.0000	90.0000	90.0000
<i>Volume</i> (Å ³)	1893.20	1891.73	1890.96
<i>Z</i>	2	2	2

Table S2 Crystal data and structure refinement for Bi-MOFs (continued).

	Bi-MOF-COOH	Bi-MOF-F	Bi-MOF-Cl
Chemical formula	$\text{Bi}_2\text{O}(\text{H}_2\text{O})_2(\text{C}_{14}\text{H}_4\text{O}_8)$	$\text{Bi}_2\text{O}(\text{H}_2\text{O})_2(\text{C}_{13}\text{H}_3\text{O}_6\text{F})$	$\text{Bi}_2\text{O}(\text{H}_2\text{O})_2(\text{C}_{13}\text{H}_3\text{O}_6\text{Cl})$
Formula weight	770.204	744.186	760.636
Crystal system	Tetragonal	Tetragonal	Tetragonal
Space group	P42	P42	P42
a (Å)	19.2456	19.2518	19.2476
b (Å)	19.2456	19.2518	19.2476
c (Å)	5.11018	5.10893	5.11011
α (Å)	90.0000	90.0000	90.0000
β (Å)	90.0000	90.0000	90.0000
γ (Å)	90.0000	90.0000	90.0000
Volume (Å ³)	1892.77	1893.54	1893.15
Z	2	2	2

Table S2 Crystal data and structure refinement for Bi-MOFs (continued).

	Bi-MOF-Br	Bi-MOF-I
Chemical formula	$\text{Bi}_2\text{O}(\text{H}_2\text{O})_2(\text{C}_{13}\text{H}_3\text{O}_6\text{Br})$	$\text{Bi}_2\text{O}(\text{H}_2\text{O})_2(\text{C}_{13}\text{H}_3\text{O}_6\text{I})$
Formula weight	805.086	852.086
Crystal system	Tetragonal	Tetragonal
Space group	P42	P42
a (Å)	19.2461	19.2415
b (Å)	19.2461	19.2415
c (Å)	5.11099	5.11233
α (Å)	90.0000	90.0000
β (Å)	90.0000	90.0000
γ (Å)	90.0000	90.0000
Volume (Å ³)	1893.17	1892.77
Z	2	2

Table S3 Lennard-Jones parameters and atomic partial charges for adsorbates and adsorbents [10-14].

Molecule	Gas models				Frameworks		
	Atom	σ (Å)	ϵ (K)	q (e)	Atom	σ (Å)	ϵ (K)
CO ₂	C	2.80	27.00	0.748	C	3.47	47.85
	O	3.05	79.00	-0.374	H	2.85	7.65
C ₂ H ₂	C	3.80	57.868	-0.278	O	3.03	48.16
	H			0.278	N	3.26	38.95
C ₂ H ₄	CH ₂	3.72	83	0.85	F	3.09	36.48
	COM			-1.70	Cl	3.52	142.56
					Br	3.52	186.18
					I	3.70	256.63
				Bi	3.89	260.66	

Table S4 Adsorption capacities of C₂H₄, C₂H₂, and CO₂ in Bi-MOF materials at 298

K and different pressures (in mmol/g).

		Bi-MOF-H	-CHO	-COOH	-NO ₂	-F	-Cl	-Br	-I
1 kPa	C ₂ H ₄	0.06	0.18	0.11	0.10	0.13	0.07	0.11	0.10
	C ₂ H ₂	0.05	0.95	0.31	0.27	0.32	0.24	0.23	0.14
	CO ₂	0.07	1.30	0.56	0.27	0.10	0.06	0.13	0.13
100 kPa	C ₂ H ₄	1.60	1.29	1.22	1.18	1.40	1.20	1.19	1.10
	C ₂ H ₂	2.30	1.38	1.28	1.25	1.58	1.25	1.18	1.08
	CO ₂	2.58	2.49	1.90	2.13	2.51	1.67	1.75	1.43

Table S5 Metrics relevant to equimolar CO₂/C₂H₄ separation for Bi-MOFs in comparison to typical CO₂-selective MOFs at 298 K and 100 kPa reported until now.

Adsorbent	Pore size (Å)	Uptake of CO ₂ /C ₂ H ₄ ^a	Q_{st} of CO ₂ /C ₂ H ₄ ^b	CO ₂ /C ₂ H ₄ selectivity	Ref.
MUF-16	3.6~7.6	2.14/0.14	32/24.9	600 ^c	[15]
MUF-16(Mn)	3.6~7.6	2.25/0.37	36.6/-	150 ^c	[15]
MUF-16(Ni)	3.6~7.6	2.14/0.24	37.3/-	130 ^c	[15]
Bi-MOF-CHO	5.8	2.49/1.29	48.2/34.6	58.6	This work
Qc-5-Cu	3.3	2.48/0.74	36.2/23.1	39.95 ^d	[16]
Zn(5NO ₂ -ip)(dpe)	-	1.98/1.43	-	14.56 ^d	[17]
Bi-MOF-COOH	6.0	1.90/1.22	43.6/30.6	10.3	This work
Bi-MOF-NO ₂	6.2	2.13/1.18	38.8/30.7	10.6	This work
SU-101(Al)	5.1	2.37/0.98	31.3/25.8	8.3 ^f	[18]
SU-101	6.6	2.40/0.97	34.3/24.4	8.1 ^f	[18]
Zn-atz-oba	3.2~4.4	2.50/2.03	29.0/27.0	1.33	[19]
Mg-MOF-74	10.2	8.86/8.03	-	1.13 ^d	[16]
ZNU-6	8.22~10.76	4.76/~4.7	37.1/~29.0	7.8 ^d	[6]
TIFSIX-17-Ni	3.6	2.1/0.3	37.8/27.4 ^f	7 ^e	[20]
ZJU-197a	3.7~6.8	1.20/0.53	24.1/47.8	2.28 ^e	[21]
F-PYMO-Cu	3.4	1.41/0.014	53.5/-	100.7 ^e	[22]

^a Gas uptake (mmol/g). ^b Q_{st} at low coverage (kJ/mol). ^c At 293 K. ^d Selectivity of CO₂/C₂H₄ (1/99, v/v). ^e Uptake ratio of CO₂/C₂H₄ at 100 kPa. ^f Calculated from Monte Carlo simulations.

Table S6 Metrics relevant to equimolar CO₂/C₂H₂ separations for Bi-MOFs in comparison to typical CO₂-selective MOFs at 298 K and 100 kPa reported until now.

Adsorbent	Pore size (Å)	Uptake of CO ₂ /C ₂ H ₂ ^a	Q _{st} of CO ₂ /C ₂ H ₂ ^b	CO ₂ /C ₂ H ₂ selectivity	Ref.
Zn-ox-mtz	3.8	3.07/0.24	43.02/~38	1064.9	[23]
MUF-16	3.6~7.6	2.14/0.18	32/25.8	510 ^c	[15]
Cd-NP	3.2	2.58/0.43	27.7/-	85	[24]
MUF-16(Ni)	3.6~7.6	2.14/0.34	37.3/-	46 ^c	[15]
MUF-16(Mn)	3.6~7.6	2.25/0.43	36.6/-	31 ^c	[15]
Tm-MOF(1a) ^d	6.1	5.83/2.1	45.2/17.8	17.5 ^e	[25]
SU-101(Al)	5.1	2.37/0.88	31.3/24.8	15.5 ^f	[18]
SU-101(Ga)	5.5	1.80/0.69	27.7/23.5	11.1 ^f	[18]
[Mn(bdc)(dpe)]	-	2.08/0.32	29.5/27.8	9 ^g	[26]
Bi-MOF-CHO	5.8	2.49/1.38	48.2/46.2	7.7	This work
SIFSIX-3-Ni	3.8	2.80/3.30	50.9/36.7	7.7 ^e	[27]
CD-MOF-2	4.8	2.67/2.03	67.2/25.8	6.1	[28]
SU-101	6.6	2.40/2.29	34.3/16.1	5.5	[18]
Bi-MOF-COOH	6.0	1.90/1.28	43.6/40.6	5.3	This work
Bi-MOF-NO ₂	6.2	2.13/1.25	38.8/38.5	4.9	This work
F-PYMO-Cu	3.4	1.61/0.89	53.5/35.9	3.7	[22]
CD-MOF-1	5.2	2.87/2.23	41/17.6	3.4	[28]
Zn-MOF ^h	5.7~7.8	34.6 ⁱ /18.0 ⁱ	32.7/25.4	2.4	[29]
Tm-MOF(1a') ^d	6.2	6.21/5.25	32.7/26.0	1.65 ^e	[25]

^a Gas uptake (mmol/g). ^b Q_{st} at low coverage (kJ/mol). ^c 293 K and 100 kPa. ^d [Tm₂(OH-bdc)₂(μ₃-OH)₂(H₂O)₂]. ^e Selectivity of CO₂/C₂H₂ (1/2, v/v). ^f Calculated from Monte Carlo simulations. ^g 273 K and 100 kPa. ^h [Zn(atz)(BDC-Cl₄)_{0.5}]_n. ⁱ Volumetric uptake (cm³/cm³)

Table S7 Comparison of pore size, gas uptake, and IAST selectivity among reported MOFs used in one-step C₂H₄ purification from ternary CO₂/C₂H₂/C₂H₄ mixtures.

	Pore size (Å)	Uptake ^a		Selectivity ^b		Ref.
		CO ₂ /C ₂ H ₂ /C ₂ H ₄	CO ₂ /C ₂ H ₄	C ₂ H ₂ /C ₂ H ₄		
Bi-MOF-CHO	5.8	2.49/1.38/1.29	58.6	11.8	This work	
Bi-MOF-COOH	6.0	1.90/1.28/1.22	10.3	3.1	This work	
Bi-MOF-NO ₂	6.2	2.13/1.25/1.18	10.6	2.2	This work	
Zn-atz-oba	3.2~4.4	2.50/2.77/2.03	1.33	1.43	[19]	
NTU-67	4.95	2.04/3.29/1.41	10.8	8.1	[30]	
NTU-65 ^c	5.5	3.55/3.85/0.10	-	-	[31]	
TIFSIX-17-Ni	3.6	2.1/3.3/0.3	-	670.9	[20]	
SIFSIX-17-Ni	3.5	2.3/3.3/0.6	-	506.4	[20]	
ZNU-6	8.2~10.9	4.76/8.06/~4.7	7.84 ^d	8.19 ^d	[6]	

^a Gas uptake (mmol/g). ^b IAST selectivity with the ratio of 50/50. ^c Flexible MOF. ^d Henry's selectivity.

Table S8 Productivities of purified C₂H₄, containing less than 40 ppm impurity (C₂H₂) for 1/1/98 C₂H₂/CO₂/C₂H₄ mixture separations with Bi-MOFs. The unit of productivities are expressed in mol/kg and cm³/cm³ respectively.

	Simulations including diffusion		Simulations ignoring diffusion	
	in mol/kg	in cm ³ /cm ³	in mol/kg	in cm ³ /cm ³
Bi-MOF-CHO	6.1	400.41	11.5	754.87
Bi-MOF-NO ₂	0.15	10.07	1.3	87.26
Bi-MOF-COOH	0.18	12.04	1.75	117.04

Table S9 Productivities of purified C₂H₄, containing less than 40 ppm impurity (C₂H₂), for 1/9/90 C₂H₂/CO₂/C₂H₄ mixture separations with Bi-MOFs. The unit of productivities are expressed in mol/kg and cm³/cm³ respectively.

	Simulations including diffusion		Simulations ignoring diffusion	
	in mol/kg	in cm ³ /cm ³	in mol/kg	in cm ³ /cm ³
Bi-MOF-CHO	5.2	341.33	9.7	636.71
Bi-MOF-NO ₂	0.14	9.40	1.27	85.25
Bi-MOF-COOH	0.18	12.04	1.7	113.69

Table S10 Comparison of C₂H₄ productivity from C₂H₂/CO₂/C₂H₄ (1/9/90) mixtures among reported porous adsorbents.

	Crystal density (g/cm ³)	C ₂ H ₄ productivity		Ref.
		in mol/kg	in cm ³ /cm ³	
Bi-MOF-CHO	2.65	5.2	341.33	This work
ZNU-6	1.074	13.81	367.39	[6]
NTU-67	1.289	5.42	173.05	[30]
SIFSIX-17-Ni	-	2.47	-	[20]
SIFSIX-2-Cu-i	1.247	2.40	74.13	[6]
Activated carbon	-	0.49	-	[6]
Zeolite 5A	-	0.36	-	[6]

Fig. S1

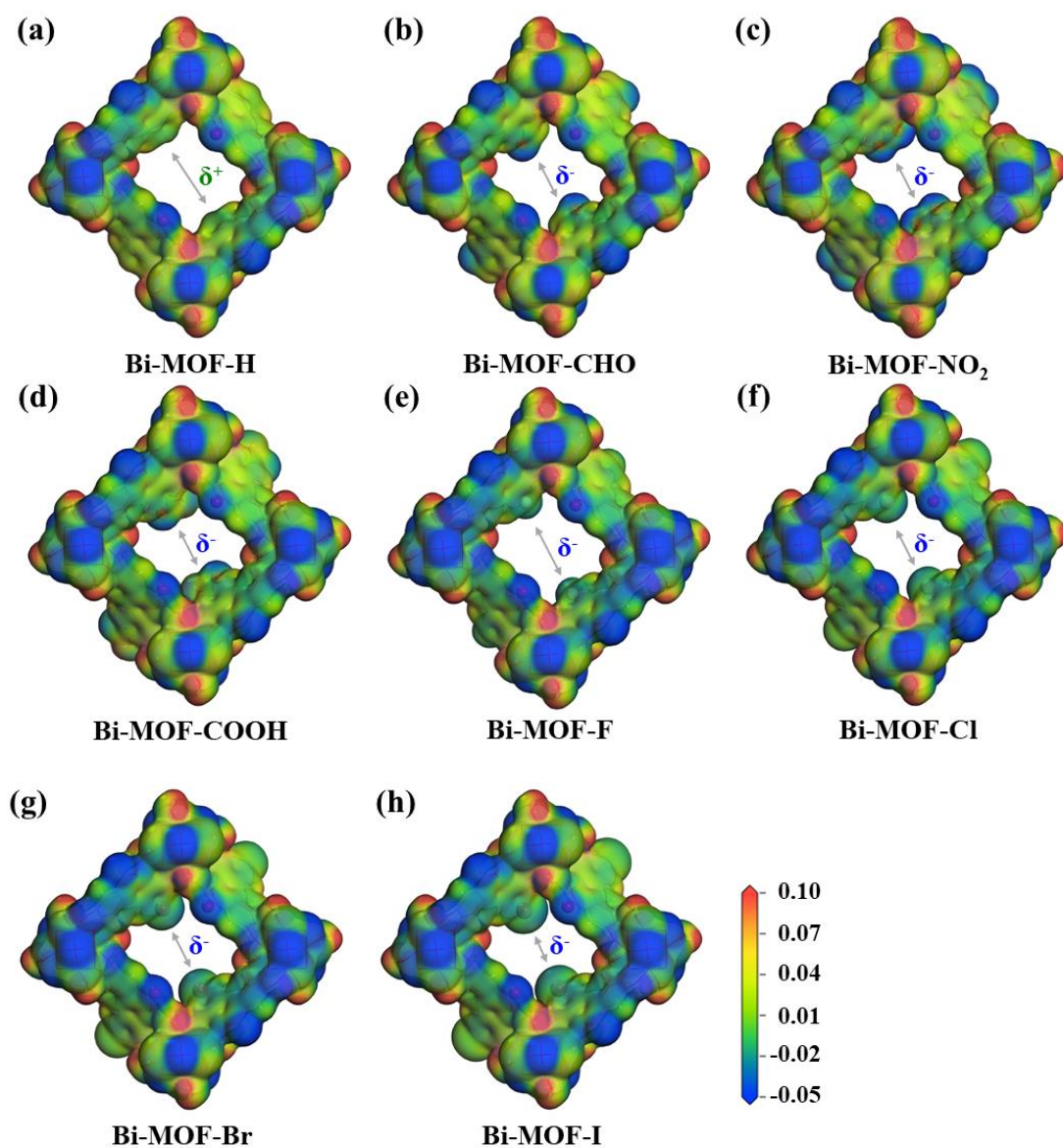


Fig. S1 Electrostatic potential maps of channel surface of Bi-MOF materials. The isovalue of electron density distribution is $0.017 \text{ e}/\text{\AA}^3$.

Fig. S2

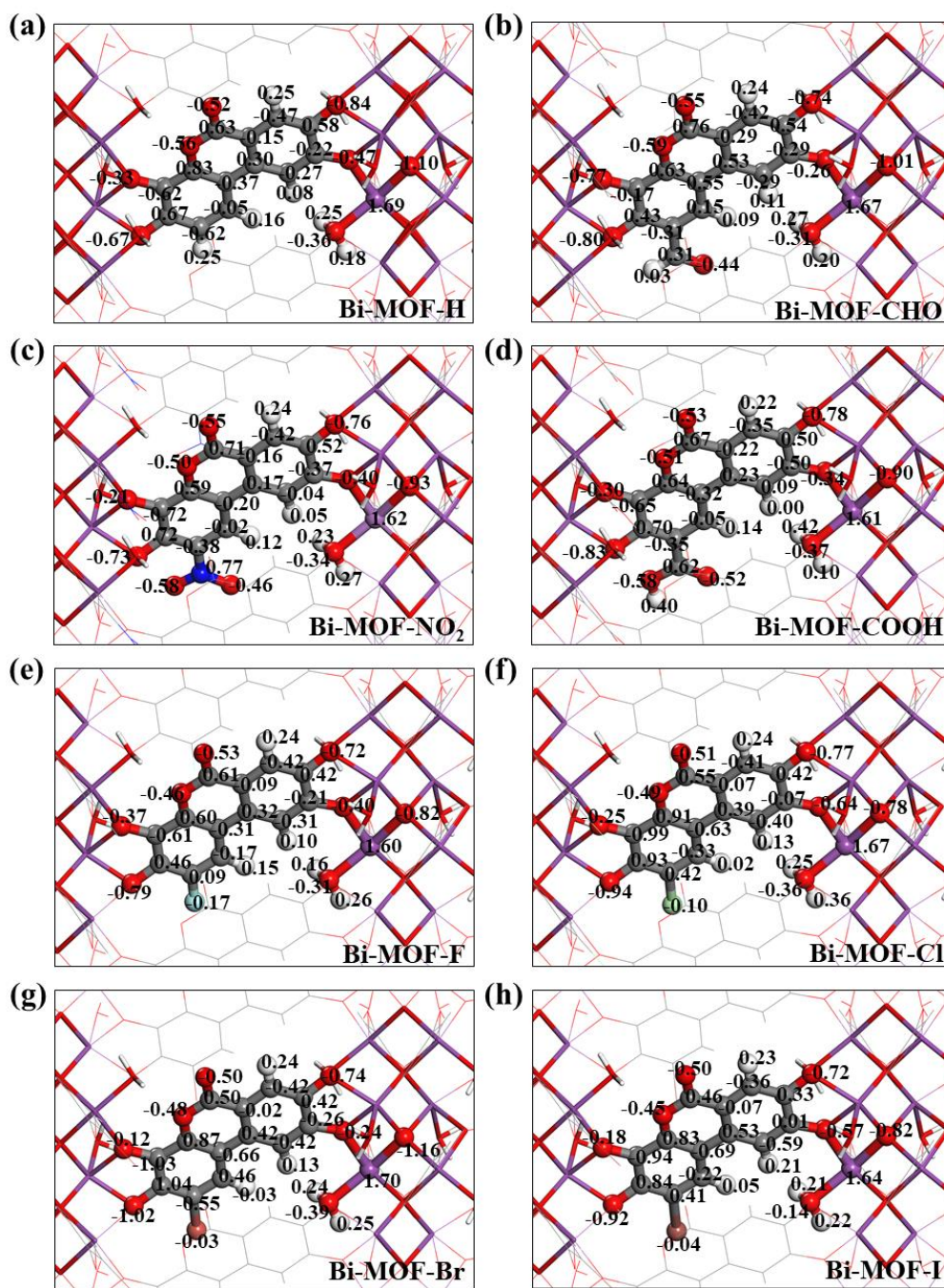


Fig. S2 DFT-derived atomic partial charges (in e) of Bi-MOF structures.

Fig. S3

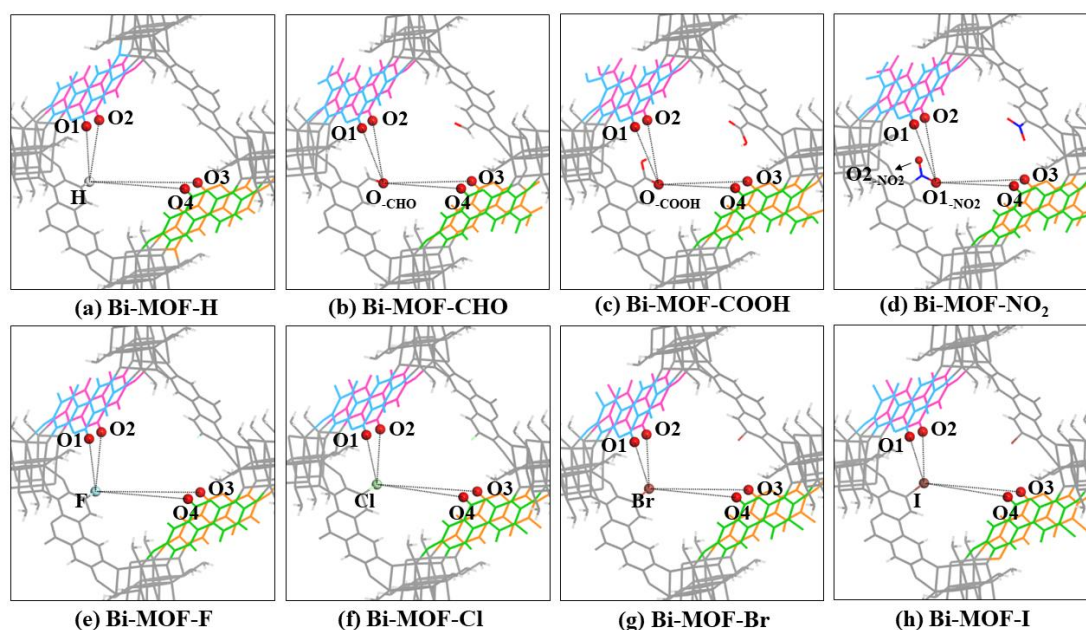


Fig. S3 Structures of channel surfaces in Bi-MOF materials and the positional relationship of various surface electronegative atoms. The relevant **X-O** distances (in Å) are listed in the below table.

	-H	-CHO	-COOH	-NO ₂	-F	-Cl	-Br	-I
X-O1	5.59	6.10	6.23	6.29	5.57	5.45	5.40	5.33
X-O2	5.10	5.14	5.26	5.30	4.90	4.56	4.43	4.27
X-O3	8.49	7.02	7.03	7.00	8.29	7.97	7.85	7.69
X-O4	8.79	7.75	7.78	7.78	8.71	8.51	8.43	8.23

X represents the H atom in Bi-MOF-H and the electronegative atoms (marked in the structure diagram) from various functional groups exposed to channel surfaces. In Bi-MOF-NO₂, **X** represents the O atom named O1-NO₂. **O1-O4** atoms are all from the carbonyl groups.

Fig. S4

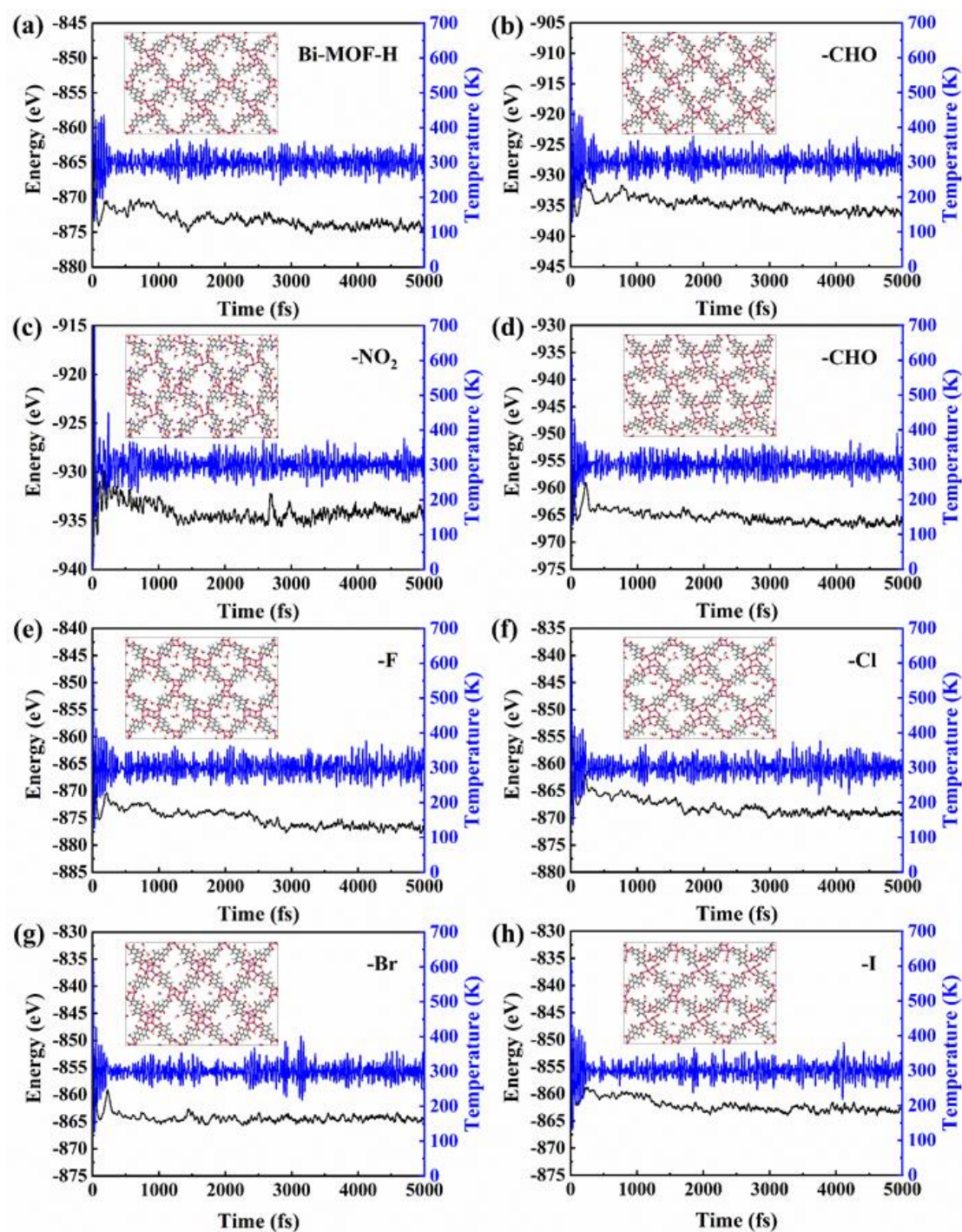


Fig. S4 AIMD simulations of the total energy (black) and system temperature (blue) in the process of Bi-MOF structural evolution. The insets are the snapshots of Bi-MOFs at 5000 fs.

Fig. S5

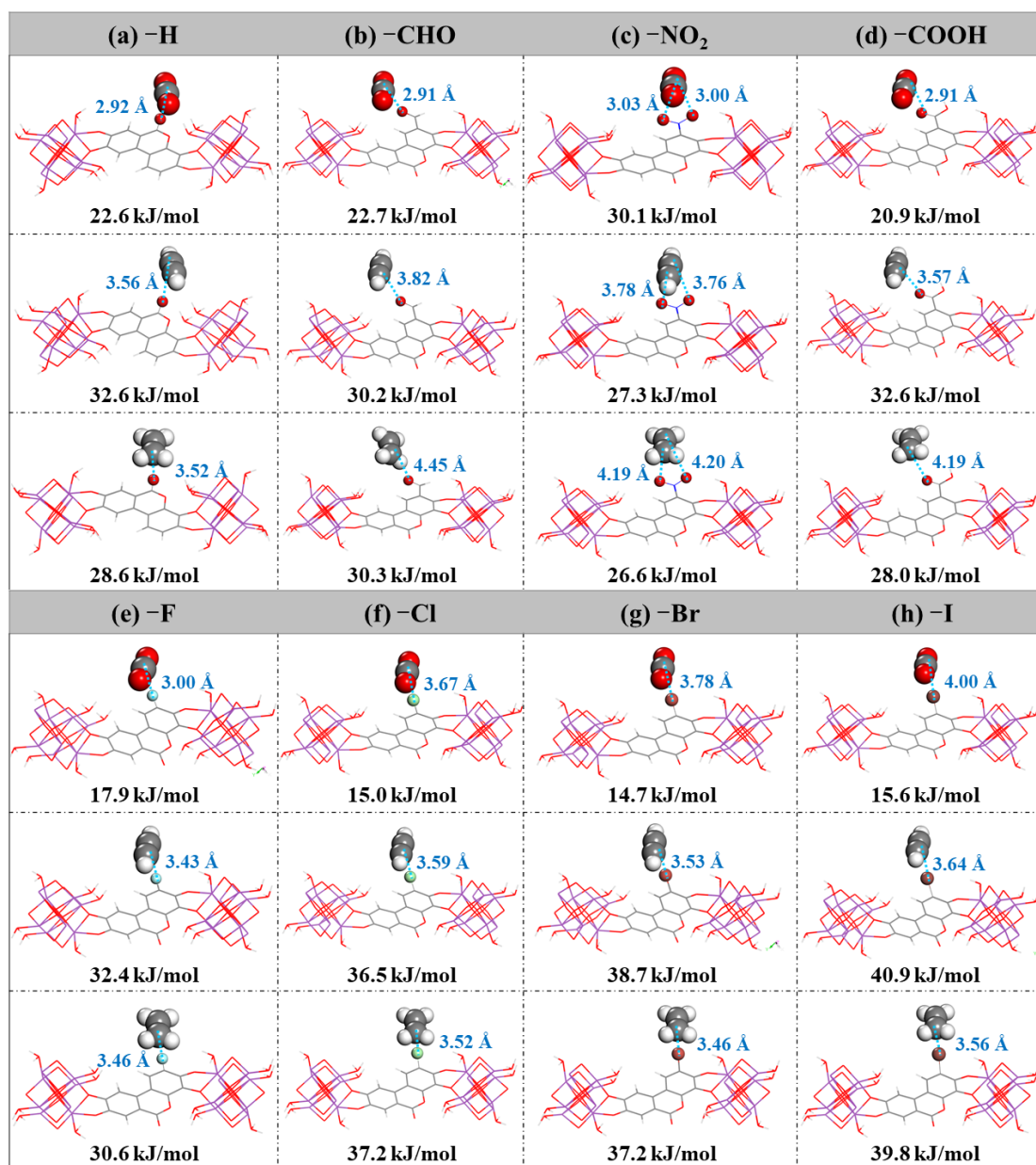


Fig. S5 DFT calculated adsorption configurations and energies of CO₂, C₂H₂, and C₂H₄ at the electronegative atoms from ligand carbonyl and functional groups in Bi-MOF materials.

Fig. S6

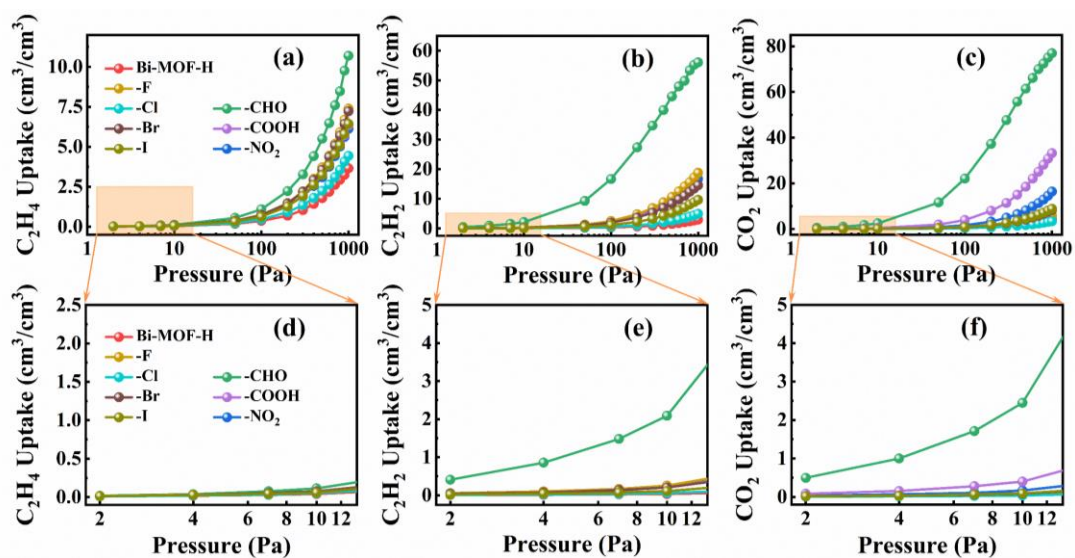


Fig. S6 Adsorption isotherms of C₂H₄, C₂H₂, and CO₂ in Bi-MOF materials at 298 K and different pressure ranges: (a-c) 2-1000 Pa; (d-f) 2-12 Pa.

Fig. S7

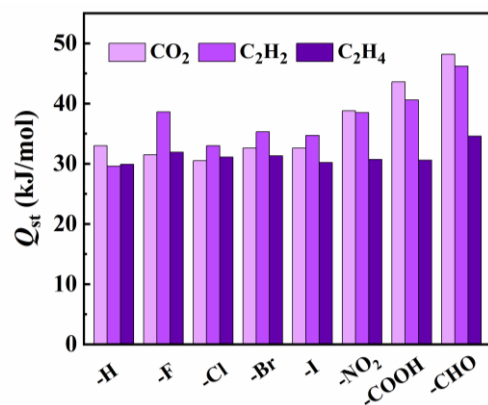


Fig. S7 The isosteric heats of adsorption of CO₂, C₂H₂, and C₂H₄ in Bi-MOF materials near zero-coverage at 298 K.

Fig. S8

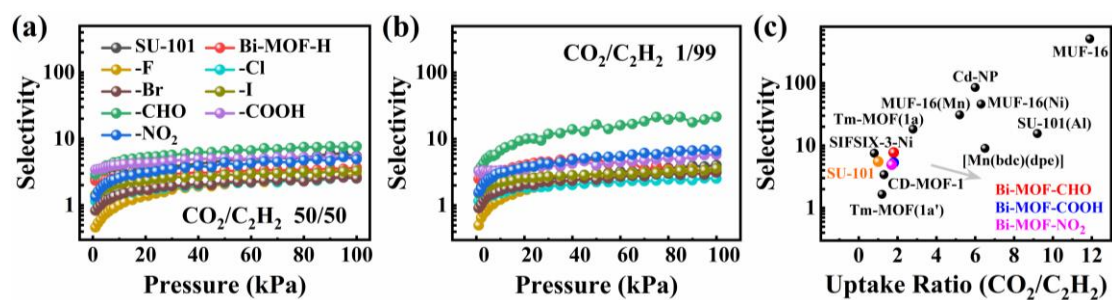


Fig. S8 (a,b) $\text{CO}_2/\text{C}_2\text{H}_2$ selectivity in Bi-MOFs at 298 K under 50/50 and 1/99 and (c) comparison of the selectivity and corresponding uptake ratio at 100 kPa for equimolar $\text{CO}_2/\text{C}_2\text{H}_2$ between functionalized Bi-MOFs and other top-performance materials at atmospheric temperatures (see details in Table S6).

Fig. S9

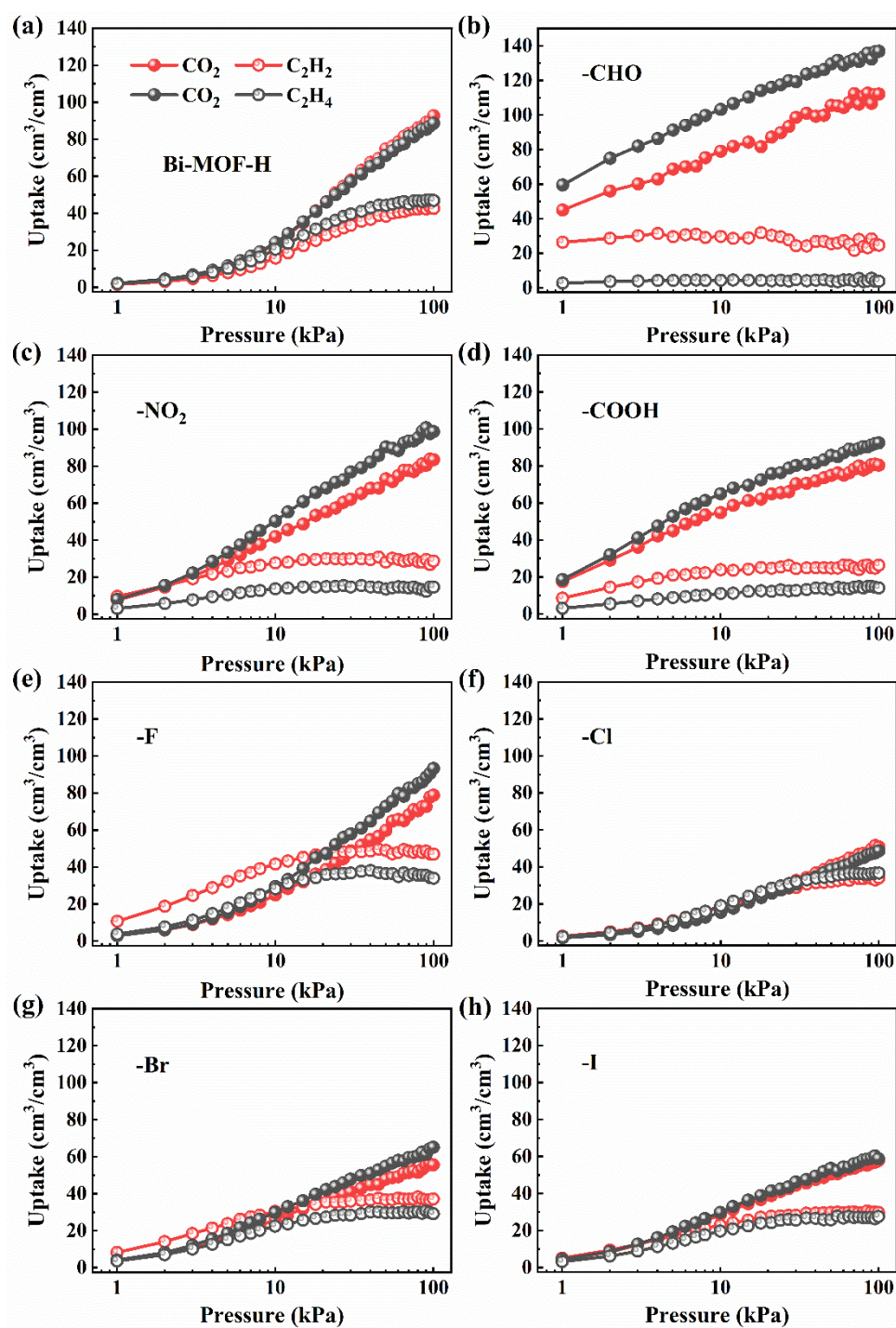


Fig. S9 Adsorption amounts of component gases from equimolar $\text{CO}_2/\text{C}_2\text{H}_2$ and $\text{CO}_2/\text{C}_2\text{H}_4$ mixtures in Bi-MOFs at 298 K.

Fig. S10

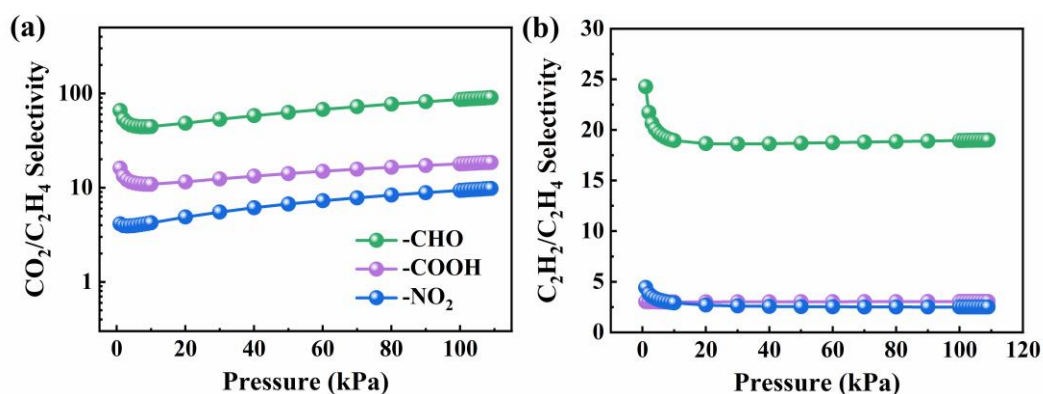


Fig. S10 IAST selectivity of Bi-MOF-CHO, Bi-MOF-COOH, and Bi-MOF-NO₂ for equimolar mixtures based on single-component gas isotherms from GCMC simulations.

Langmuir-Freundlich fit parameters:

For calculating IAST selectivity, adsorption isotherms for CO₂, C₂H₂, and C₂H₄ in Bi-MOFs were first fitted to the single-site Langmuir-Freundlich model:

$$q = Q_{sat} \frac{b_1 P^{c_1}}{1 + b_1 P^{c_1}},$$

where q is the gas capacity (mmol/g) at gas pressure (kPa); Q_{sat} is the theoretical maximum gas capacities (mmol/g); b_1 is Langmuir-Freundlich constant for site 1 (kPa⁻¹); c_1 is Freundlich exponent (dimensionless). Langmuir-Freundlich fitting parameters are listed below:

	Gas	Q_{sat}	b_1	c_1
Bi-MOF-NO ₂	CO ₂	2.27507	0.16993	0.90862
	C ₂ H ₂	1.37098	0.25655	0.79765
	C ₂ H ₄	1.28537	0.08849	1.03815
Bi-MOF-COOH	CO ₂	2.05773	0.44981	0.66262
	C ₂ H ₂	1.28727	0.31856	1.19747
	C ₂ H ₄	1.27414	0.08566	1.20954
Bi-MOF-CHO	CO ₂	2.84721	0.84827	0.45277
	C ₂ H ₂	1.37815	2.3383	0.76832
	C ₂ H ₄	1.32013	0.15982	1.15486

Fig. S11

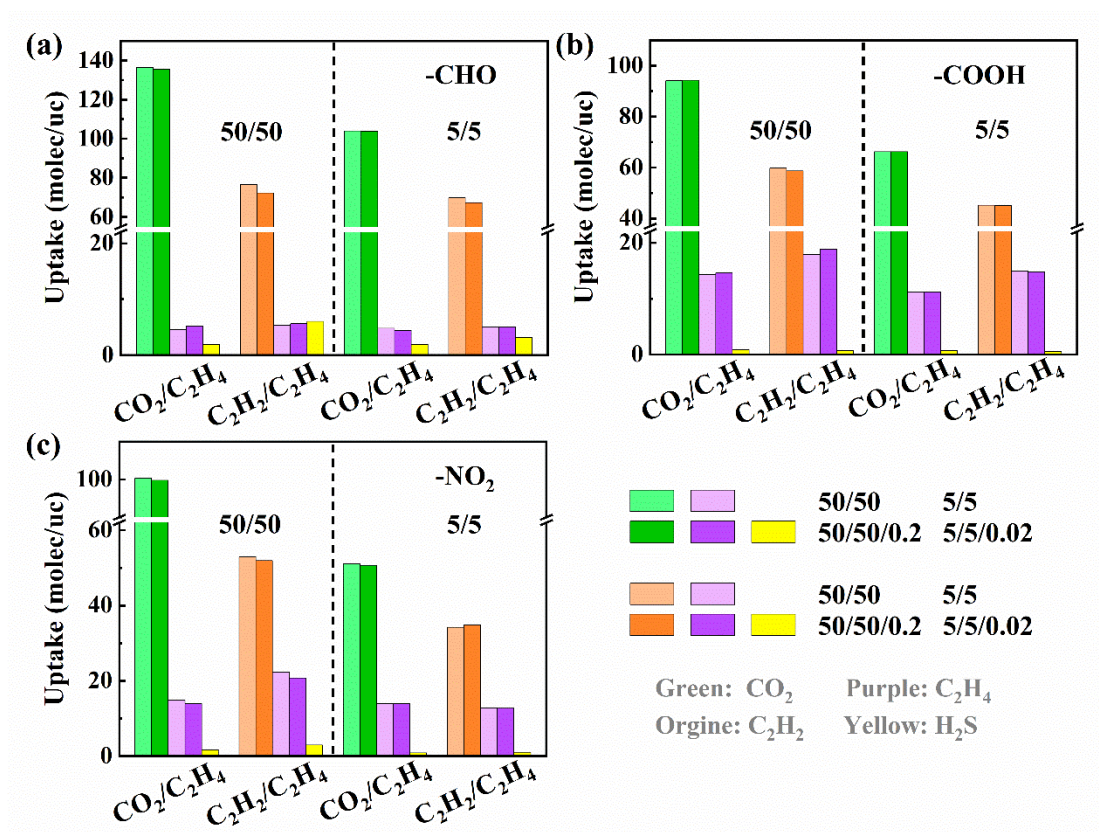


Fig. S11 Adsorption amounts of each component from $\text{CO}_2/\text{C}_2\text{H}_4$ and $\text{C}_2\text{H}_2/\text{C}_2\text{H}_4$ mixtures containing trace amount of H_2S in (a) Bi-MOF-CHO, (b) Bi-MOF-COOH, and (c) Bi-MOF-NO₂ at 298 K and different pressures (10 kPa and 100 kPa). The molar composition of H_2S (0.002, 2000 ppm) was selected based on the prototypical examples of real natural gas, biogas, and flue gases [32]. The ratios of $\text{CO}_2/\text{C}_2\text{H}_4/\text{H}_2\text{S}$ and $\text{C}_2\text{H}_2/\text{C}_2\text{H}_4/\text{H}_2\text{S}$ mixtures were 50/50/0.2 (100 kPa) and 5/5/0.02 (10 kPa) respectively.

Fig. S12

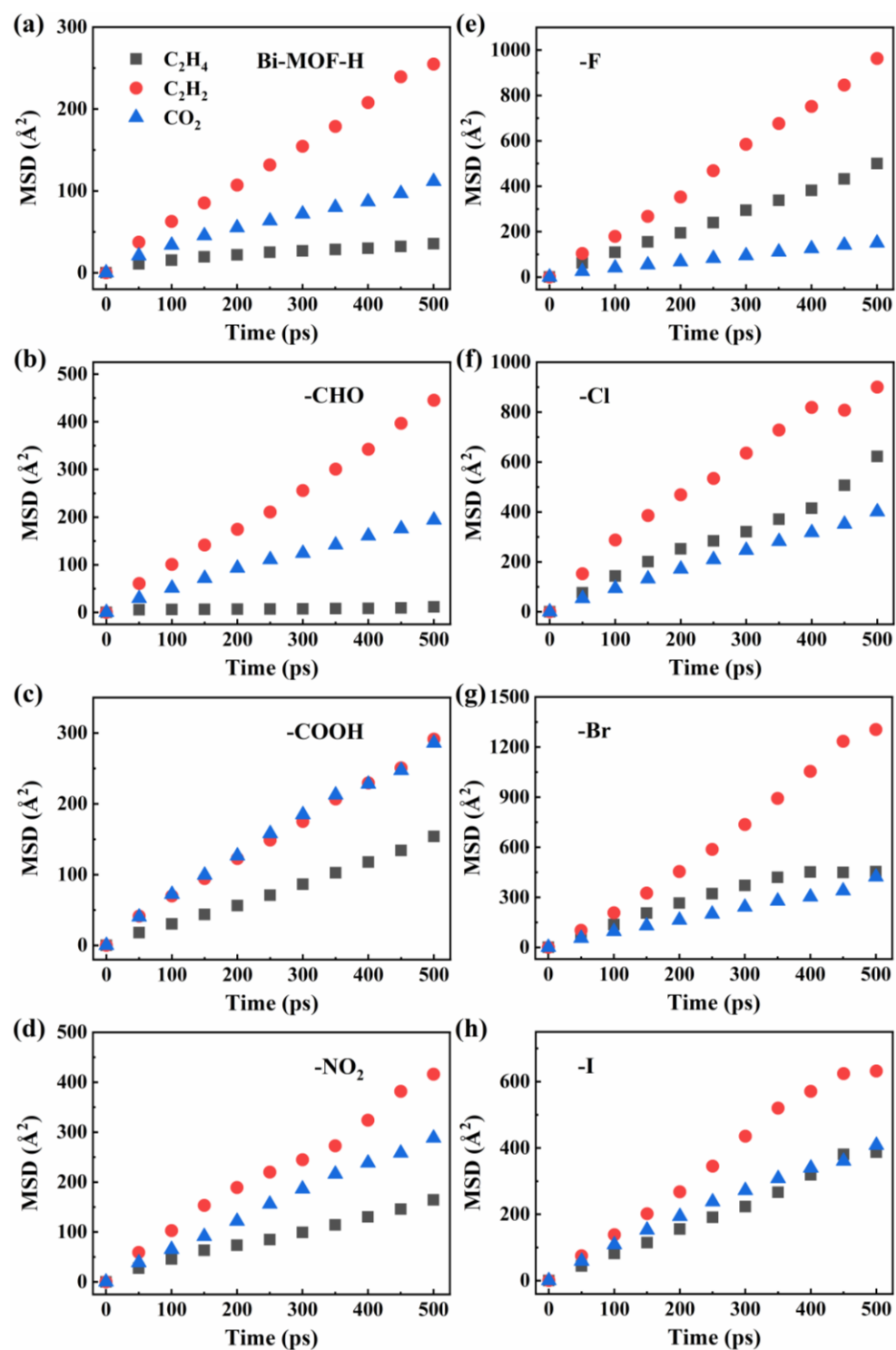


Fig. S12 Mean square displacement (MSD) vs mean simulation time diagrams for diffusion of single-component C_2H_4 , C_2H_2 , and CO_2 in various functionalized Bi-MOFs at 298 K.

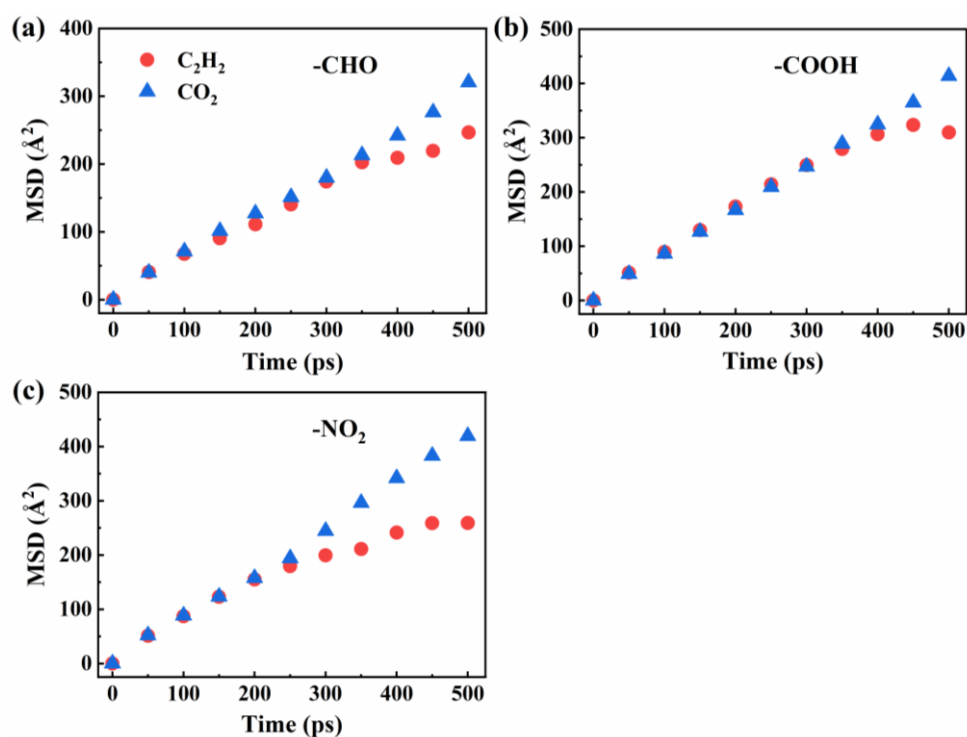
Fig. S13

Fig. S13 Mean square displacement (MSD) vs mean simulation time diagrams for diffusion of equimolar $\text{CO}_2/\text{C}_2\text{H}_2$ mixture in -CHO, -COOH, and - NO_2 functionalized MOFs at 298 K. The relevant diffusion coefficient of single-component C_2H_4 , C_2H_2 , and CO_2 in Bi-MOFs, as well as equimolar $\text{CO}_2/\text{C}_2\text{H}_2$ mixture in Bi-MOF-CHO/-COOH/- NO_2 , are listed in the below table (298 K, in $10^{-9} \text{ m}^2/\text{s}$).

	-H	-CHO	- NO_2	-COOH	-F	-Cl	-Br	-I
CO_2	0.34	0.62	0.96	0.91	1.59	1.84	1.59	1.31
C_2H_2	0.83	1.42	1.31	0.92	3.20	2.90	4.55	2.26
C_2H_4	0.10	0.02	0.51	0.47	0.49	1.29	1.29	1.32
$\text{CO}_2_{\text{bin}}^a$		1.01	1.35	1.40				
$\text{C}_2\text{H}_2_{\text{bin}}^a$		0.81	1.11	0.85				

^a From binary $\text{CO}_2/\text{C}_2\text{H}_2$ mixture.

Fig. S14

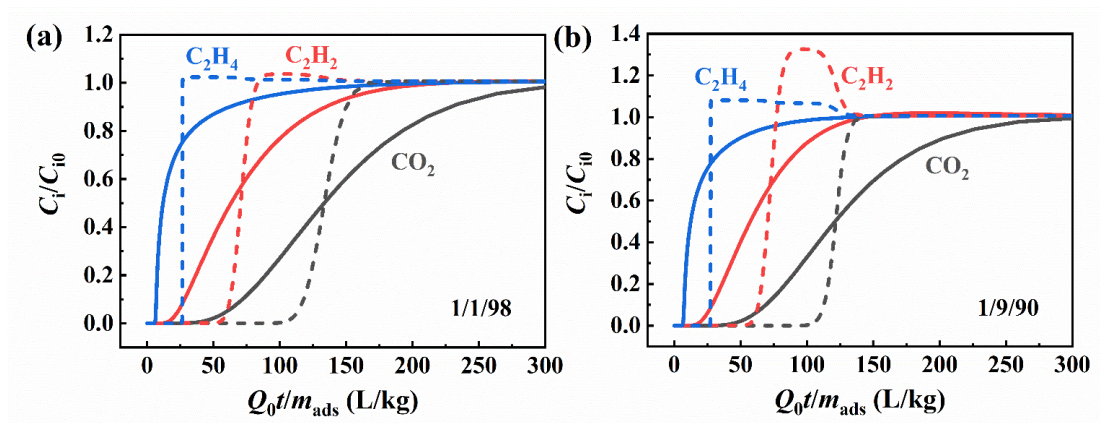


Fig. S14 Transient breakthrough simulations for (a) 1/1/98 $C_2H_2/CO_2/C_2H_4$, and (b) 1/9/90 $C_2H_2/CO_2/C_2H_4$ mixtures in fixed bed packed with Bi-MOF- NO_2 . The continuous solid lines represent simulations in which due account is taken of diffusional influences. The dashed lines are the simulations in which diffusional influences are considered to be negligible.

Fig. S15

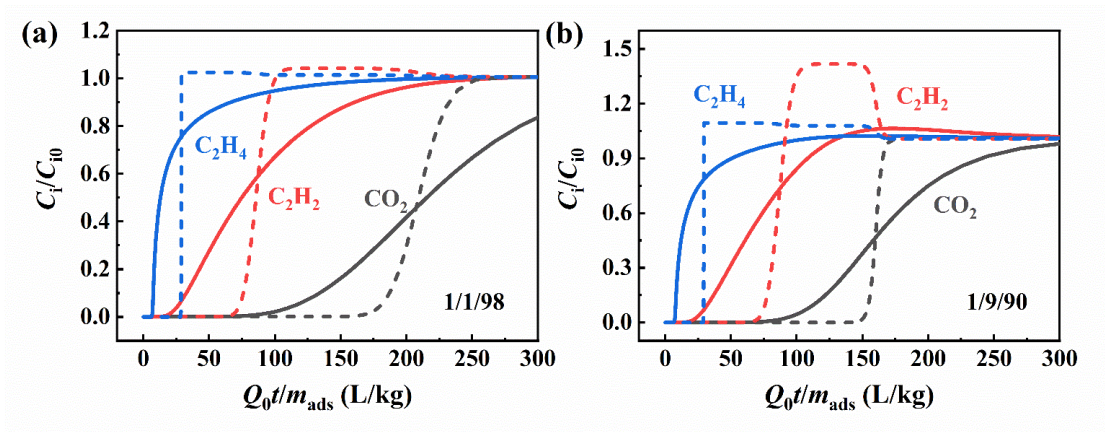


Fig. S15 Transient breakthrough simulations for (a) 1/1/98 $\text{C}_2\text{H}_2/\text{CO}_2/\text{C}_2\text{H}_4$, and (b) 1/9/90 $\text{C}_2\text{H}_2/\text{CO}_2/\text{C}_2\text{H}_4$ mixtures in fixed bed packed with Bi-MOF-COOH. The continuous solid lines represent simulations in which due account is taken of diffusional influences. The dashed lines are the simulations in which diffusional influences are considered to be negligible.

Fig. S16

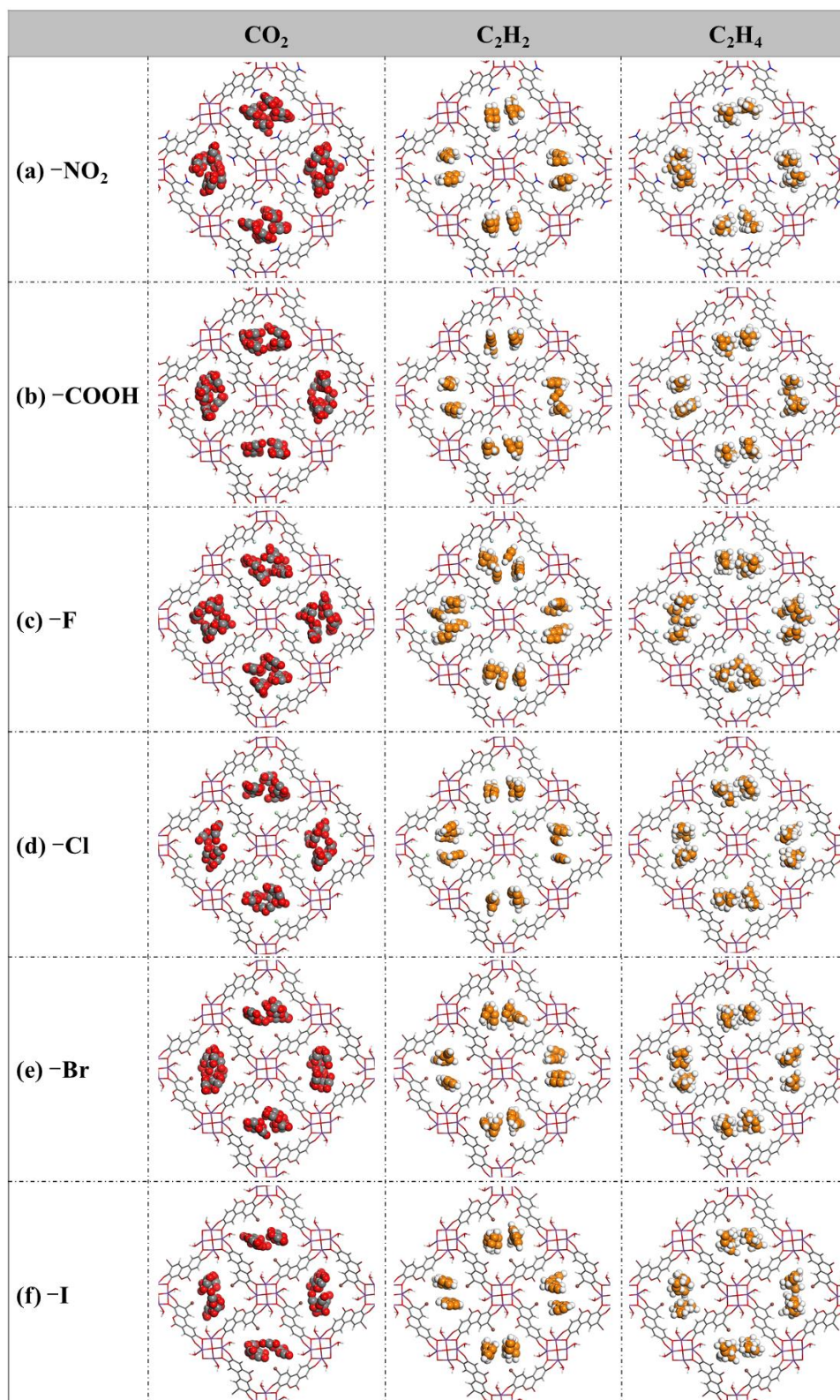


Fig. S16 Snapshots of CO_2 , C_2H_2 , and C_2H_4 in various functionalized Bi-MOFs at 298

K and 100 kPa.

Fig. S17

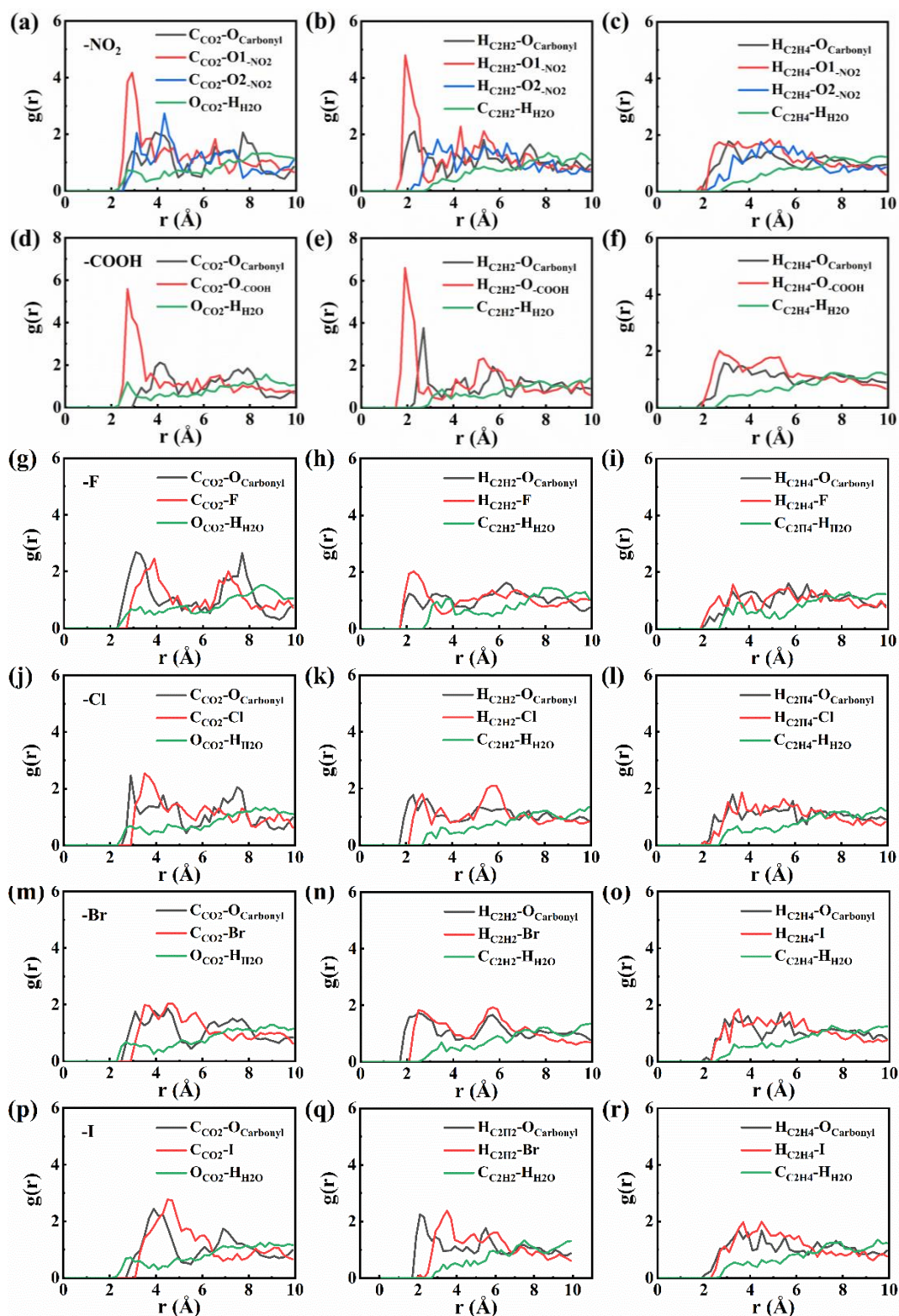


Fig. S17 Radial distribution functions of CO₂, C₂H₂, and C₂H₄ in various functionalized

Bi-MOFs at 298 K and 100 kPa.

Fig. S18

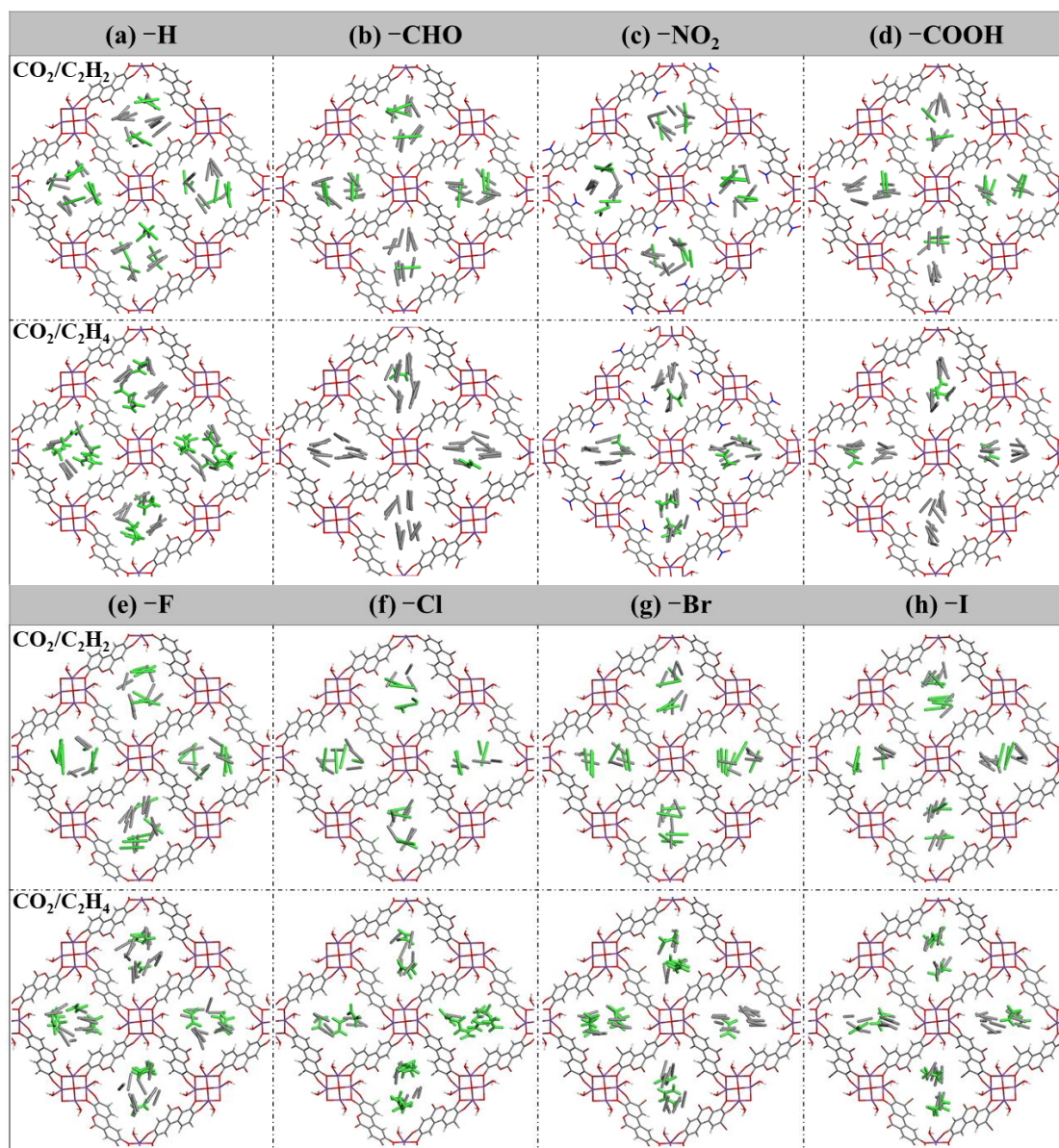


Fig. S18 Snapshots of CO₂/C₂H₂ and CO₂/C₂H₄ mixtures in Bi-MOFs at 298 K and 100 kPa (Gray, CO₂; Green, C₂H₂ or C₂H₄).

Fig. S19

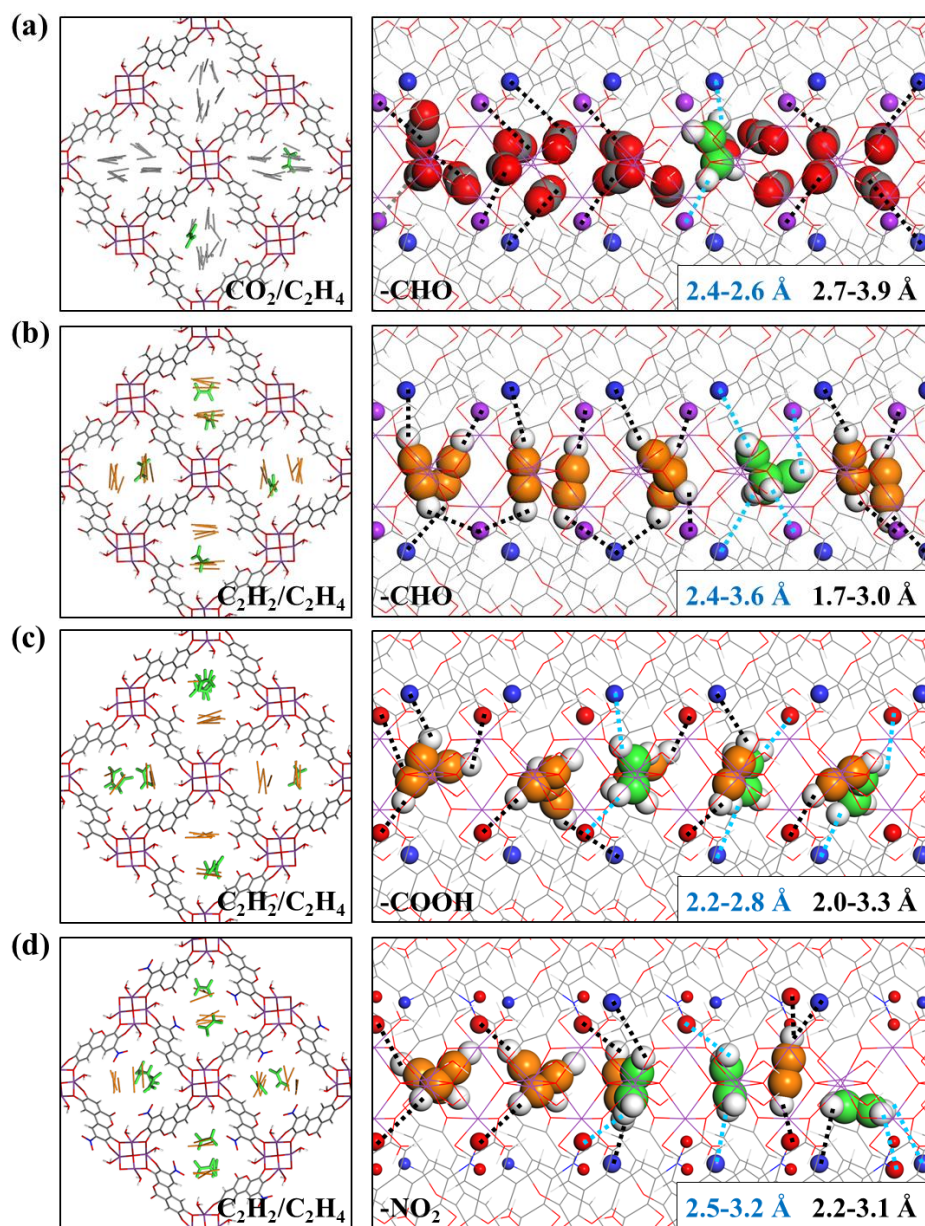


Fig. S19 Snapshots of equimolar mixtures in functionalized Bi-MOFs at 298 K and 100 kPa (Blue, O_{Carbonyl}; Purple/Red, O_{Functional}). Five unit cells along the channel direction are shown. Top view: CO₂, Grey; C₂H₂, Orange; C₂H₄, Green.

Fig. S20

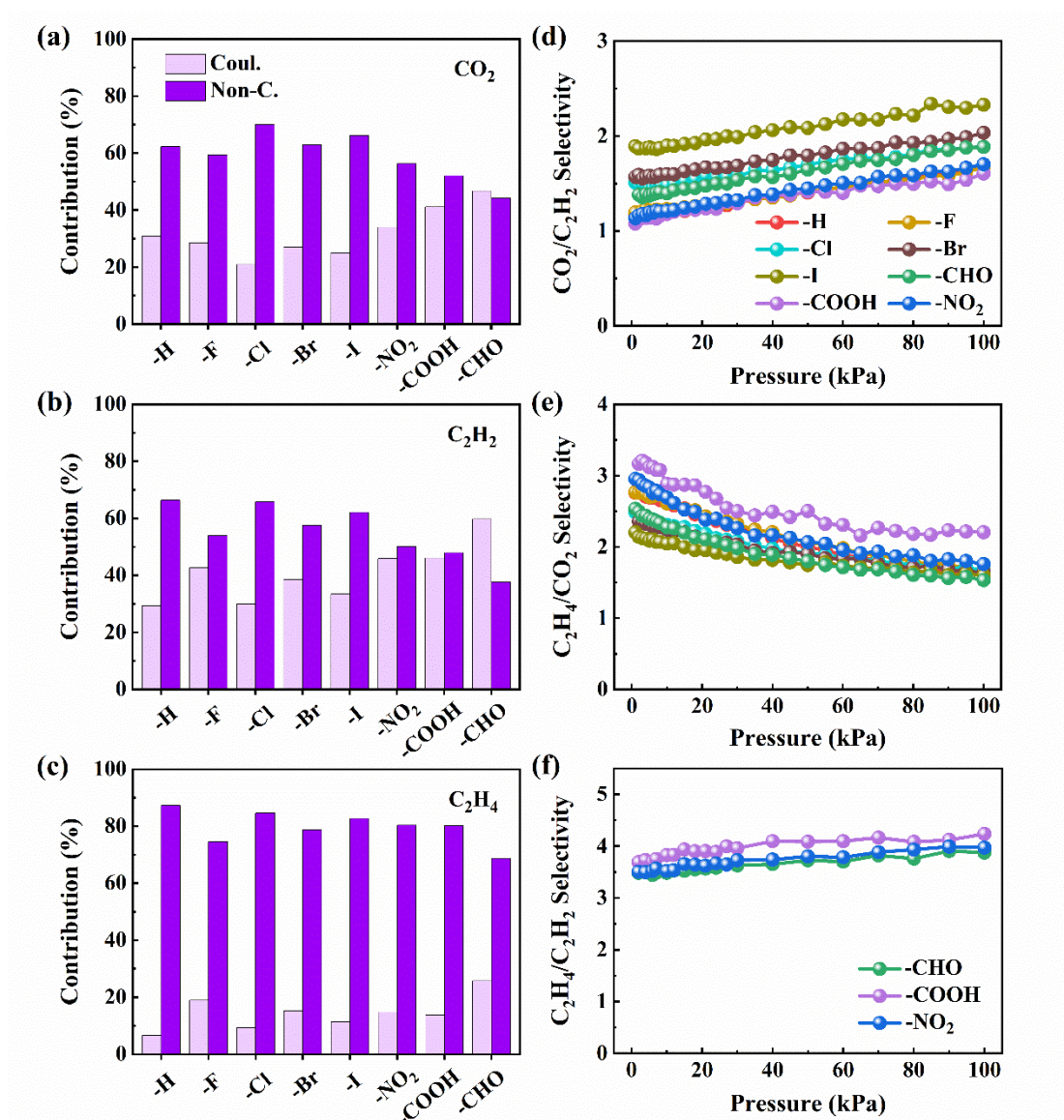


Fig. S20 (a-c) Average contribution percentages of Coulomb and non-Coulomb interactions between adsorbates and Bi-MOFs at 298 K. (d-f) Selectivities of equimolar CO₂/C₂H₂, CO₂/C₂H₄, and C₂H₂/C₂H₄ mixtures without considering Coulomb interactions between adsorbates and Bi-MOFs.

References

- [1] R. Krishna, Screening metal–organic frameworks for mixture separations in fixed-bed adsorbers using a combined selectivity/capacity metric, *RSC Adv.* 7(57) (2017) 35724-35737.
- [2] R. Krishna, Methodologies for evaluation of metal–organic frameworks in separation applications, *RSC Adv.* 5(64) (2015) 52269-52295.
- [3] R. Krishna, The Maxwell–Stefan description of mixture diffusion in nanoporous crystalline materials, *Micropor. Mesopor. Mater.* 185 (2014) 30-50.
- [4] R. Krishna, Tracing the origins of transient overshoots for binary mixture diffusion in microporous crystalline materials, *Phys. Chem. Chem. Phys.* 18(23) (2016) 15482-15495.
- [5] R. Krishna, Synergistic and antis synergistic intracrystalline diffusional influences on mixture separations in fixed-bed adsorbers, *Precis. Chem.* 1(2) (2023) 83-93.
- [6] Y. Jiang, Y. Hu, B. Luan, L. Wang, R. Krishna, H. Ni, X. Hu, Y. Zhang, Benchmark single-step ethylene purification from ternary mixtures by a customized fluorinated anion-embedded MOF, *Nat. Commun.* 14(1) (2023) 401.
- [7] A.L. Myers, J.M. Prausnitz, Thermodynamics of mixed-gas adsorption, *AIChE J.* 11(1) (1965) 121-127.
- [8] S. Mukherjee, D. Sensharma, K.-J. Chen, M.J. Zaworotko, Crystal engineering of porous coordination networks to enable separation of C₂ hydrocarbons, *Chem. Commun.* 56(72) (2020) 10419-10441.
- [9] J.-R. Li, R.J. Kuppler, H.-C. Zhou, Selective gas adsorption and separation in metal–

- organic frameworks, *Chem. Soc. Rev.* 38(5) (2009) 1477-1504.
- [10] A.K. Rappé, C.J. Casewit, K. Colwell, W.A. Goddard III, W.M. Skiff, UFF, a full periodic table force field for molecular mechanics and molecular dynamics simulations, *J. Am. Chem. Soc.* 114(25) (1992) 10024-10035.
- [11] J.J. Potoff, J.I. Siepmann, Vapor–liquid equilibria of mixtures containing alkanes, carbon dioxide, and nitrogen, *AIChE J.* 47(7) (2001) 1676-1682.
- [12] S.L. Weitz, J.J. Potoff, Effect of quadrupole moment on the phase behavior of binary mixtures containing ethene, *Fluid Phase Equilibr.* 234(1-2) (2005) 144-150.
- [13] M. Fischer, F. Hoffmann, M. Fröba, New microporous materials for acetylene storage and C₂H₂/CO₂ separation: Insights from molecular simulations, *ChemPhysChem* 11(10) (2010) 2220-2229.
- [14] S.L. Mayo, B.D. Olafson, W.A. Goddard, DREIDING: A generic force field for molecular simulations, *J. Phys. Chem.* 94(26) (1990) 8897-8909.
- [15] O.T. Qazvini, R. Babarao, S.G. Telfer, Selective capture of carbon dioxide from hydrocarbons using a metal-organic framework, *Nat. Commun.* 12(1) (2021) 197.
- [16] T. He, Y. Xiao, Q. Zhao, M. Zhou, G. He, Ultramicroporous metal–organic framework Qc-5-Cu for highly selective adsorption of CO₂ from C₂H₄ stream, *Ind. Eng. Chem. Res.* 59(7) (2020) 3153-3161.
- [17] S. Horike, K. Kishida, Y. Watanabe, Y. Inubushi, D. Umeyama, M. Sugimoto, T. Fukushima, M. Inukai, S. Kitagawa, Dense coordination network capable of selective CO₂ capture from C₁ and C₂ hydrocarbons, *J. Am. Chem. Soc.* 134(24) (2012) 9852-9855.

- [18] C. Hao, H. Ren, H. Zhu, Y. Chi, W. Zhao, X. Liu, W. Guo, CO₂-favored metal–organic frameworks SU-101(M) (M = Bi, In, Ga, and Al) with inverse and high selectivity of CO₂ from C₂H₂ and C₂H₄, *Sep. Purif. Technol.* 290 (2022) 120804.
- [19] J.W. Cao, S. Mukherjee, T. Pham, Y. Wang, T. Wang, T. Zhang, X. Jiang, H.J. Tang, K.A. Forrest, B. Space, M.J. Zaworotko, K.J. Chen, One-step ethylene production from a four-component gas mixture by a single physisorbent, *Nat. Commun.* 12(1) (2021) 6507.
- [20] S. Mukherjee, N. Kumar, A.A. Bezrukov, K. Tan, T. Pham, K.A. Forrest, K.A. Oyekan, O.T. Qazvini, D.G. Madden, B. Space, M.J. Zaworotko, Amino-functionalised hybrid ultramicroporous materials that enable single-step ethylene purification from a ternary mixture, *Angew. Chem. Int. Ed.* 60(19) (2021) 10902-10909.
- [21] L. Zhang, K. Jiang, Y. Yang, Y. Cui, B. Chen, G. Qian, A novel Zn-based heterocycle metal-organic framework for high C₂H₂/C₂H₄, CO₂/CH₄ and CO₂/N₂ separations, *J. Solid State Chem.* 255 (2017) 102-107.
- [22] X. Jiang, T. Pham, J.W. Cao, K.A. Forrest, H. Wang, J. Chen, Q.Y. Zhang, K.J. Chen, Molecular sieving of acetylene from ethylene in a rigid ultra-microporous metal-organic framework, *Chem. Eur. J.* 27(36) (2021) 9446-9453.
- [23] S.-Q. Yang, R. Krishna, H. Chen, L. Li, L. Zhou, Y.-F. An, F.-Y. Zhang, Q. Zhang, Y.-H. Zhang, W. Li, T.-L. Hu, X.-H. Bu, Immobilization of the polar group into an ultramicroporous metal–organic framework enabling benchmark Inverse selective CO₂/C₂H₂ separation with record C₂H₂ production, *J. Am. Chem. Soc.* (2023). <https://doi.org/10.1021/jacs.3c03265>.

- [24] Y. Xie, H. Cui, H. Wu, R.B. Lin, W. Zhou, B. Chen, Electrostatically driven selective adsorption of carbon dioxide over acetylene in an ultramicroporous material, *Angew. Chem. Int. Ed.* 60(17) (2021) 9604-9609.
- [25] D. Ma, Z. Li, J. Zhu, Y. Zhou, L. Chen, X. Mai, M. Liufu, Y. Wu, Y. Li, Inverse and highly selective separation of CO₂/C₂H₂ on a thulium–organic framework, *J. Mater. Chem. A* 8(24) (2020) 11933-11937.
- [26] M.L. Foo, R. Matsuda, Y. Hijikata, R. Krishna, H. Sato, S. Horike, A. Hori, J. Duan, Y. Sato, Y. Kubota, M. Takata, S. Kitagawa, An adsorbate discriminatory gate effect in a flexible porous coordination polymer for selective adsorption of CO₂ over C₂H₂, *J. Am. Chem. Soc.* 138(9) (2016) 3022-3030.
- [27] K.-J. Chen, H.S. Scott, D.G. Madden, T. Pham, A. Kumar, A. Bajpai, M. Lusi, K.A. Forrest, B. Space, J.J. Perry, M.J. Zaworotko, Benchmark C₂H₂/CO₂ and CO₂/C₂H₂ separation by two closely related hybrid ultramicroporous materials, *Chem* 1(5) (2016) 753-765.
- [28] L. Li, J. Wang, Z. Zhang, Q. Yang, Y. Yang, B. Su, Z. Bao, Q. Ren, Inverse adsorption separation of CO₂/C₂H₂ mixture in cyclodextrin-based metal-organic frameworks, *ACS Appl. Mater. Interfaces* 11(2) (2019) 2543-2550.
- [29] X.-Y. Li, Y. Song, C.-X. Zhang, C.-X. Zhao, C. He, Inverse CO₂/C₂H₂ separation in a pillared-layer framework featuring a chlorine-modified channel by quadrupole-moment sieving, *Sep. Purif. Technol.* 279 (2021) 119608.
- [30] Q. Dong, Y. Huang, K. Hyeon-Deuk, I.Y. Chang, J. Wan, C. Chen, J. Duan, W. Jin, S. Kitagawa, Shape- and size-dependent kinetic ethylene sieving from a ternary

mixture by a trap-and-flow channel crystal, *Adv. Funct. Mater.* 32(38) (2022) 2203745.

[31] Q. Dong, X. Zhang, S. Liu, R.-B. Lin, Y. Guo, Y. Ma, A. Yonezu, R. Krishna, G. Liu, J. Duan, R. Matsuda, W. Jin, B. Chen, Tuning gate-opening of a flexible metal–organic framework for ternary gas sieving separation, *Angew. Chem. Int. Ed.* 59(50) (2020) 22756-22762.

[32] X. Peng, D. Cao, Computational screening of porous carbons, zeolites, and metal organic frameworks for desulfurization and decarburization of biogas, natural gas, and flue gas, *AIChE J.* 59(8) (2013) 2928-2942.